

SEMDOT: Smooth-Edged Material Distribution for Optimizing Topology Algorithm

Yun-Fei Fu^a, Bernard Rolfe^a, Louis N. S. Chiu^b, Yanan Wang^a, Xiaodong Huang^c, Kazem Ghabraie^{a,*}

^a*School of Engineering, Deakin University, Warrnambool, VIC 3217, Australia*

^b*Department of Materials Science and Engineering, Monash University, Clayton, VIC 3800, Australia*

^c*Faculty of Science, Engineering and Technology, Swinburne University of Technology, Hawthorn, VIC 3122, Australia*

Abstract

Element-based topology optimization algorithms capable of generating smooth boundaries have drawn serious attention given the significance of accurate boundary information in engineering applications. The basic framework of a new element-based continuum algorithm is proposed in this paper. This algorithm is based on a smooth-edged material distribution strategy that uses solid/void grid points assigned to each element. Named Smooth-Edged Material Distribution for Optimizing Topology (SEMDOT), the algorithm uses elemental volume fractions which depend on the densities of grid points in the Finite Element Analysis (FEA) model rather than elemental densities. Several numerical examples are studied to demonstrate the application and effectiveness of SEMDOT. In these examples, SEMDOT proved to be capable of obtaining optimized topologies with smooth and clear boundaries showing better or comparable performance compared to other topology optimization methods. Through these examples, first, the advantages of using the Heaviside smooth function are discussed in comparison to the Heaviside step function. Then, the benefits of introducing multiple filtering steps in this algorithm are shown. Finally, comparisons are conducted to exhibit the differences between SEMDOT and some well-established element-based algorithms. The validation of the sensitivity analysis method adopted in SEMDOT is conducted using a typical compliant mechanism design case. In addition, this paper provides the Matlab code of SEMDOT for educational and academic purposes.

Keywords: Topology optimization, Smooth design, Elemental volume fractions, Boundary elements, Heaviside smooth function, Matlab code

1. Introduction

Topology optimization basically aims to distribute a given amount of material within a predefined design domain such that optimal or near optimal structural performance can be obtained [1, 2, 3]. It often provides highly efficient designs that could not be obtained by simple intuition without assuming any prior structural configuration. Topology optimization as a design method has been greatly developed and extensively used since the pioneering paper on numerical topology optimization by Bendsoe and Kikuchi [4]. A number of topology optimization algorithms have been proposed based on different strategies: homogenization of microstructures [4], using elemental densities as design variables [5], evolutionary approaches [6], topological derivative [7], level-set (LS) [8, 9], phase field [10], moving morphable component (MMC) [11], moving morphable void (MMV) [12], elemental volume fractions [13], and using the floating projection [14, 15]. In recent years, these topology optimization approaches have been applied in a wide range of distinct engineering problems, including frequency responses [16, 17], stress problems [18, 19], convection problems [20, 21, 22], structural failure problems [23, 24], large-scale problems [25, 26, 27], nanophotonics

*Corresponding author: email: k.ghabraie@deakin.edu.au, Tel: +61 3 524 79574

[28], metamaterial design [29], and manufacturing oriented methods [30, 31, 32, 33, 34] have been presented in recent years.

Early proposed topology optimization algorithms are mainly element-based such as solid isotropic material with penalization (SIMP) algorithm [35] and bi-directional evolutionary structural optimization (BESO) algorithm [36]. SIMP uses the artificial power-law function between elemental densities and material properties to suppress intermediate elements to a solution with black and white elements, and BESO heuristically updates design variables using discrete values (0 and 1). As elements are not only involved in finite element analysis (FEA) but the formation of topological boundaries, zigzag (for example, BESO) or both zigzag and blurry boundaries (for example, SIMP) will be inevitably generated. Therefore, shape optimization or other post-processing methods have to be used to obtain accurate boundary information after topology optimization [37, 38, 39]. Given the significance of the accurate boundary representation, some proposed algorithms such as the level-set method, MMC-based method, elemental volume fractions based method, and using the floating projection have successfully solved the boundary issue. Even though there are a number of algorithms capable of forming smooth or high resolution boundaries, element-based algorithms that could combine the benefits of different methods are generally preferred because of their advantages of easy implementation and ability of creating holes freely across the design domain and obtaining final topologies that are not heavily dependent on the initial guess [14].

Elemental volume fractions based methods are originally from the evolutionary topology optimization (ETO) algorithms using the continuation method on the volume and BESO-based optimizer [13, 40, 41, 42]. To provide a more easy-to-use, flexible, and efficient optimization platform, the authors proposed a new smooth continuum topology optimization algorithm through combining the benefits of the smooth representation in ETO and density-based optimization in SIMP [43, 44, 45, 46]. The proposed algorithm is termed Smooth-Edged Material Distribution for Optimizing Topology (SEMDOT) based on its optimization mechanism. The basic idea of elemental volume fractions based algorithms (for example, ETO and SEMDOT) is to pursue the solid/void design of grid points that are assigned to each element through which smooth boundaries can be obtained. The concept of using design points within an element has been proposed and studied before ETO and SEMDOT. Nguyen et al. [47] presented a multiresolution topology optimization (MTOP) scheme that can generate high resolution designs with relatively low computational cost using three different meshes: the displacement mesh, density mesh, and design variable mesh. In MTOP, Gauss points were used for the integration of the stiffness matrix. Afterwards, Park and Sutradhar [48] first used MTOP to obtain high resolution designs for 3D multi-material problems. However, Gupta et al. [49] pointed out that the complexity of MTOP would restrict its attractiveness to students and scholars. Instead of using design points within each element, Kang and Wang [50] proposed a pointwise density-based interpolation method where the density field is constructed from design points within a certain circular influence domain of the point. Unlike ETO and SEMDOT, design points in the method proposed by Kang and Wang [50] are not involved in forming smooth boundaries, so the non-smooth boundary issue persists in it.

Compared with some newly developed or improved algorithms capable of generating smooth boundaries, SEMDOT can be easily integrated with some existing methods that were established based on SIMP to achieve specific performance goals. An example is the combination of SEMDOT and Langelaar’s additive manufacturing (AM) filter [51] which can successfully generate smooth self-supporting topologies [43, 45, 52]. Other than Langelaar’s AM filter, some other strategies regarding AM restrictions proposed by van de Ven et al. [53] and Zhang et al. [54] can also be considered in SEMDOT for the support-free design. However, extra efforts have to be made for MMCs-based methods to obtain self-supporting designs [55]. In addition, the effectiveness of SEMDOT in solving 3D optimization problems is recently demonstrated by Fu et al. [46], through solving a number of benchmark problems and a comparison with a well-established large-scale topology optimization framework, TopOpt (proposed by Aage et al. [25]).

Even though the theoretical framework of SEMDOT was built and demonstrated by authors, other benefits and distinctions of SEMDOT compared with some current element-based algorithms have not been thoroughly discussed. Furthermore, details of SEMDOT algorithm and some of its subtle differences with methods like ETO which translate into more robust performance have not been discussed before.

In this work, the reason behind using the Heaviside smooth function in SEMDOT instead of the Heaviside step function that is extensively used in ETO algorithms is explained. Effects of different combinations of filter radii on performance, convergence, and topologies, which have not been discussed in authors' previous works, are investigated, and the rationality of the sensitivity analysis strategy used in SEMDOT is proved through a compliant mechanism design case. Numerical comparisons with other element-based topology optimization methods are thoroughly conducted. Finally, the Matlab code of SEMDOT is released to the topology optimization community facilitating the replication of the results presented in this paper, and also for future use.

An overview of this paper is as follows. Section 2 explains the mathematical framework of SEMDOT. Section 3 conducts several numerical examples to exhibit the benefits and distinctions of SEMDOT compared with a number of element-based topology optimization algorithms. Concluding remarks are drawn in Section 4. Finally, the Matlab code of SEMDOT is presented in the Appendix.

2. Formulation

2.1. Mathematical descriptions of smooth-edged material distribution strategy

The smooth-edged material distribution strategy in SEMDOT is to form a clear topological boundary based on the solid/void design of grid points that are assigned to each element, as illustrated in Figure 1. In Figure 1, the density of the g th grid point in the e th element $\rho_{e,g}$ is assigned 1 to represent a solid grid point or a small artificial value ρ_{\min} (typically 0.001) to represent a void grid point. In SEMDOT, densities at grid points ($\rho_{e,g}$) are actually the design variables. Following the power-law model in SIMP, the material interpolation scheme at grid points is expressed by

$$E_e(\rho_{e,g}) = \rho_{e,g}^p E^1 \quad (1)$$

where $E_e(\rho_{e,g})$ is the function of the Young's modulus with respect to grid point densities, E^1 is the Young's modulus of the base material, and p is a penalty coefficient.

These grid point densities are not directly involved in Finite Element Analysis (FEA). Instead, in SEMDOT, element-based variables are used in the FEA model. Elemental volume fractions that depend on the densities at grid points are defined as

$$X_e = \frac{1}{N} \sum_{g=1}^N \rho_{e,g} \quad (2)$$

where X_e is the volume fraction of the e th element and N is the total number of grid points in each element. Even though the number of grid points is much higher than elements, because grid points are not involved in FEA, SEMDOT can maintain a proper balance between the smoothness of topological boundaries and computational cost.

As illustrated in Figure 1 and Equation 2, in solid or void elements, grid point densities are homogeneously distributed. Based on Equation 1, for solid and void elements we can write

$$E_e(X_e) = X_e^p E^1 \quad X_e \in \{\rho_{\min}, 1\} \quad (3)$$

In SEMDOT, the Young's modulus and stiffness matrices of solid and void elements are calculated using the standard SIMP expressions based on Equation 3. However, unlike SIMP, the intermediate (boundary) elements in

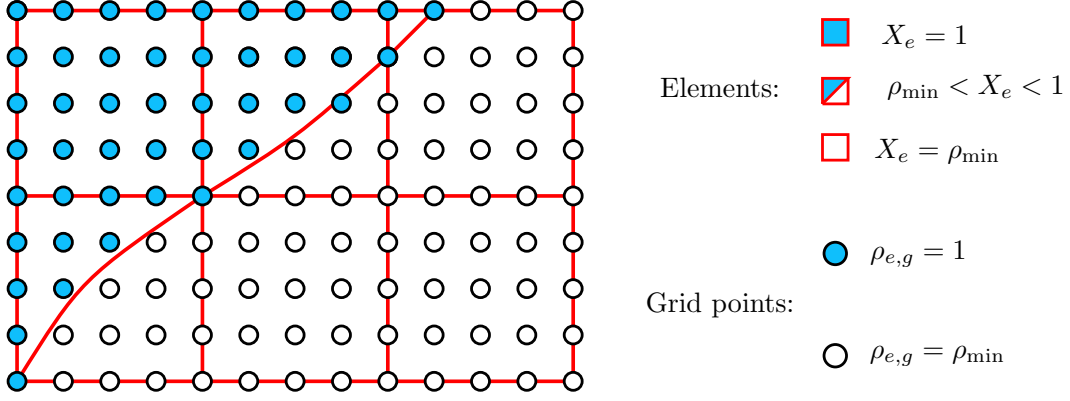


Figure 1: Illustration of smooth-edged material distribution

SEMDOT are non-homogenised combination of solid and void materials (bi-material elements), as illustrated in Figure 1. Because of this representation, elemental material properties are not well-defined functions of X_e [42]. Therefore, in SEMDOT such properties are approximated using a linear interpolation between the two phases of solid and void in the form, $\square = (1 - X_e)\square_{\text{void}} + X_e\square_{\text{solid}}$ where X_e and $(1 - X_e)$ can be regarded as weighting factors of solid and void materials, respectively. This linear interpolation scheme is used in this version of SEMDOT because of its simplicity. Based on the above discussion, the elemental stiffness matrix can be estimated as

$$\begin{aligned}\mathbf{K}_e(X_e) &= (1 - X_e)\mathbf{K}_e^0 + X_e\mathbf{K}_e^1 \\ &= (1 - X_e)\rho_{\min}^p\mathbf{K}_e^1 + X_e\mathbf{K}_e^1, \quad X_e \in [\rho_{\min}, 1]\end{aligned}\quad (4)$$

where $\mathbf{K}_e(X_e)$ is the function of the stiffness matrix with respect to the elemental volume fraction X_e , \mathbf{K}_e^0 is the stiffness matrix of the void element, and \mathbf{K}_e^1 is the stiffness matrix of the solid element.

The sensitivity measures the effectiveness of altering elemental volume fractions on reducing or increasing the objective function through which the search direction of optimization can be determined [56, 57]. Instead of calculating the sensitivities with respect to $\rho_{e,g}$, we can find the sensitivities with respect to X_e as auxiliary variables and then find $\rho_{e,g}$ values based on X_e in a later stage.

Assuming compliance as the objective function (see Section 2.2), for void and solid elements, based on Equation 3, the sensitivities with respect to X_e can be calculated as $\partial C(X_e)/\partial X_e|_{X_e=\rho_{\min}} = -p\rho_{\min}^{p-1}\mathbf{u}_e^T\mathbf{K}_e^1\mathbf{u}_e$ and $\partial C(X_e)/\partial X_e|_{X_e=1} = -p\mathbf{u}_e^T\mathbf{K}_e^1\mathbf{u}_e$, respectively. On the other hand, calculating the accurate sensitivities of boundary (intermediate) elements in SEMDOT with respect to X_e is impossible as these boundary elements are not homogeneous. Therefore, similar to what noted for material properties above, sensitivities of boundary elements are approximated as a linear combination of the sensitivities of void elements with a weighting factor of $(1 - X_e)$ and sensitivities of solid elements with a weighting factor of X_e , i.e.

$$\begin{aligned}\frac{\partial C(X_e)}{\partial X_e} &\approx (1 - X_e)\frac{\partial C(X_e)}{\partial X_e}\bigg|_{X_e=\rho_{\min}} + X_e\frac{\partial C(X_e)}{\partial X_e}\bigg|_{X_e=1} \\ &= -p[(1 - X_e)\rho_{\min}^{p-1} + X_e]\mathbf{u}_e^T\mathbf{K}_e^1\mathbf{u}_e, \quad X_e \in [\rho_{\min}, 1]\end{aligned}\quad (5)$$

where C is the objective function and \mathbf{u}_e is the displacement vector of the e th element. It is noted that Equation 5 represents the sensitivity analysis of the compliance minimization problem. The validity of this approximation can be verified through numerical examples in Section 3.

2.2. Topology optimization problems

The minimum compliance (the maximum stiffness) optimization problem, one of the most popular test cases for topology optimization, is used to comprehensively demonstrate the algorithm mechanism of SEMDOT and conduct

numerical comparisons in this paper. The corresponding optimization problem can be stated as

$$\begin{aligned}
& \min : C(X_e) = \mathbf{f}^T \mathbf{u} \\
& \text{subject to} : \mathbf{K}(X_e) \mathbf{u} = \mathbf{f} \\
& \frac{\sum_{e=1}^M X_e V_e}{\sum_{e=1}^M V_e} - V^* \leq 0 \\
& 0 < \rho_{\min} \leq X_e \leq 1; \quad e = 1, 2, \dots, M
\end{aligned} \tag{6}$$

where \mathbf{f} and \mathbf{u} are global force and displacement vectors, respectively; \mathbf{K} is the global stiffness matrix; V_e is the volume of the e th element; V^* is the prescribed value of the allowable volume; and M is the total number of elements in the design domain.

The compliant mechanism design case is also considered to further demonstrate the effectiveness of the sensitivity analysis method (Equation 5) adopted in SEMDOT. In compliant mechanism design, single-piece flexible structures transfer an input force or displacement to another point through elastic deformation [58, 59, 60]. The corresponding optimization problem can be stated as the following mathematical program:

$$\begin{aligned}
& \min : C(X_e) = -u_{out} = -\mathbf{L}^T \mathbf{u} = \tilde{\mathbf{u}}^T \mathbf{K} \mathbf{u} \\
& \text{subject to} : \mathbf{K}(X_e) \mathbf{u} = \mathbf{f}_{in} \\
& \frac{\sum_{e=1}^M X_e V_e}{\sum_{e=1}^M V_e} - V^* \leq 0 \\
& 0 < \rho_{\min} \leq X_e \leq 1; \quad e = 1, 2, \dots, M
\end{aligned} \tag{7}$$

where \mathbf{L} is a unit length vector with zeros at all degrees of freedom except at the output point where it is one, u_{out} is the output port displacement, $\tilde{\mathbf{u}}$ is the dummy load displacement vector calculated by solving $\mathbf{K} \tilde{\mathbf{u}} = -\mathbf{L}$, and \mathbf{f}_{in} is the input force vector. Similar to Equation 5, sensitivities for compliant mechanism design can be estimated as

$$\begin{aligned}
\frac{\partial C(X_e)}{\partial X_e} & \approx (1 - X_e) \frac{\partial C(X_e)}{\partial X_e} \Big|_{X_e=\rho_{\min}} + X_e \frac{\partial C(X_e)}{\partial X_e} \Big|_{X_e=1} \\
& = p[(1 - X_e)\rho_{\min}^{p-1} + X_e] \tilde{\mathbf{u}}_e^T \mathbf{K}_e^1 \mathbf{u}_e, \quad X_e \in [\rho_{\min}, 1]
\end{aligned} \tag{8}$$

where $\tilde{\mathbf{u}}_e$ is the dummy load displacement vector of the e th element.

2.3. Filtering

Using filters in topology optimization is an effective way to ensure regularity or existence of topological designs [61]. The basic idea of filters is to substitute a (possibly) non-regular function with its regularization [61]. The filter that has the same form of the density filter is used for regularization of topology optimization problems in SEMDOT. The filtering technique for elemental volume fractions is expressed as [62]:

$$\tilde{X}_e = \frac{\sum_{l=1}^{N_e} \omega_{el} X_l}{\sum_{l=1}^{N_e} \omega_{el}} \tag{9}$$

where \tilde{X}_e is the filtered elemental volume fraction, N_e is the neighborhood set of elements within the filter domain for the e th element that is a circle centered at the centroid of this element with a predefined filter radius r_{\min} , and ω_{el} is a linear weight factor defined as

$$\omega_{el} = \max(0, r_{\min} - \Delta(e, l)) \quad (10)$$

where $\Delta(e, l)$ is the center-to-center distance of the l th element within the filter domain to the e th element. It is noted that the filter for elemental volume fractions (Equations 9 and 10) can be substituted by other filters that were developed based on standard SIMP such as the sensitivity filter presented by Sigmund [63] and the partial differential equation (PDE) filters proposed by Lazarov and Sigmund [61]. It should be noted that SEMDOT aims to obtain a topological design with intermediate (gray) elements only along boundaries instead of pursuing a pure black and white (0/1) design, which means intermediate elements are useful for the determination of smooth boundaries. Consequently, some filters suppressing intermediate elements to black and white (0/1) elements (for example, Heaviside projection filter [64], morphology based filters [62], and volume preserving Heaviside projection scheme [65]) do not suit SEMDOT.

Even though the filtering technique is applied on X_e , sensitivities with respect to X_e are still required by the optimizer to update X_e . Sensitivities of the objective functional with respect to X_e can then be calculated based on the chain rule as

$$\frac{\partial C(\tilde{X}_e)}{\partial X_l} = \sum_{e=1}^{N_l} \frac{\partial C(\tilde{X}_e)}{\partial \tilde{X}_e} \frac{\partial \tilde{X}_e}{\partial X_l} = \sum_{e=1}^{N_l} \frac{\omega_{el}}{\sum_{\varsigma=1}^{N_e} \omega_{e\varsigma}} \frac{\partial C(\tilde{X}_e)}{\partial \tilde{X}_e} \quad (11)$$

To obtain the densities of grid points, nodal densities should be obtained first in SEMDOT. Nodal densities can be obtained using a heuristic filter similar to the one presented in BESO [66]:

$$\rho_n = \frac{\sum_{e=1}^M \omega_{ne} \tilde{X}_e}{\sum_{e=1}^M \omega_{ne}} \quad (12)$$

where ρ_n is the density of the n th node and ω_{ne} is the weight factor defined as

$$\omega_{ne} = \max(0, \Upsilon_{\min} - \Delta(n, e)) \quad (13)$$

where $\Delta(n, e)$ is the distance between the n th node and the center of the e th element and Υ_{\min} is the heuristic filter radius. It is important that the heuristic filter radius Υ_{\min} in SEMDOT is set to a value not less than 1, otherwise topological designs cannot be obtained for most test cases.

2.4. Generation of smooth topological boundaries

The density at the grid point $\rho(\zeta, \eta)$ in the e th element can be obtained through linear interpolation of nodal densities ρ_n . Considering a four-node element as an example, the density of the grid point $\rho(\zeta, \eta)$ is expressed by

$$\rho(\zeta, \eta) = \sum_{\gamma=1}^4 N^\gamma(\zeta, \eta) \rho_n^\gamma \quad \text{and} \quad \rho(\zeta, \eta) \in \rho(x, y) \quad (14)$$

where (ζ, η) is the local coordinate of the grid point, ρ_n^γ is the density for the γ th node of the element, and $N^\gamma(\zeta, \eta)$ is an appropriate shape function.

Theoretically, the solid/void design of grid points can be implemented by either Heaviside step function or Heaviside smooth function. The Heaviside step function is expressed by [64]

$$\rho_{e,g} = \begin{cases} 1 & \text{if } \rho_{e,g} > \Psi \\ \rho_{\min} & \text{if } \rho_{e,g} \leq \Psi \end{cases} \quad (15)$$

where Ψ is a threshold value.

The tanh-based expression of the Heaviside smooth function proposed by Wang et al. [67] is used in SEMDOT, which is

$$\rho_{e,g} = \frac{\tanh(\beta \cdot \Psi) + \tanh[\beta \cdot (\rho(x, y) - \Psi)]}{\tanh(\beta \cdot \Psi) + \tanh[\beta \cdot (1.0 - \Psi)]} \quad (16)$$

where β is a scaling parameter that controls the steepness and is updated by

$$\beta_k = \beta_{k-1} + \Lambda \quad (17)$$

where the subscripts denote the iteration number and Λ is the evolution rate for β .

Once grid point densities are calculated, filtered elemental volume fractions are updated for the next round of FEA through summing up the grid points for each element:

$$\tilde{X}_e^{new} = \frac{1}{N} \sum_{g=1}^N \rho_{e,g}^{new} \quad (18)$$

where $\rho_{e,g}^{new}$ is the density of the grid point obtained by the Heaviside step or smooth function.

The relationship between \tilde{X}_e and \tilde{X}_e^{new} can be simply established as:

$$\delta_e = \tilde{X}_e^{new} - \tilde{X}_e \quad (19)$$

where δ_e is the deviation of \tilde{X}_e and \tilde{X}_e^{new} . Equation 19 was mentioned in [43], whereas no details were provided there. Hence comprehensive discussions regarding this relationship will be presented in Section 3.2.

The shape of the topological design is represented by a level-set function $\Phi(x, y)$:

$$\Phi(x, y) = \begin{cases} \rho(x, y) - \Psi > 0 & \text{for solid region} \\ \rho(x, y) - \Psi = 0 & \text{for boundary} \\ \rho(x, y) - \Psi < 0 & \text{for void region} \end{cases} \quad (20)$$

where (x, y) is the global coordinate of grid points, $\Phi(x, y)$ is the level-set function for grid points, and $\rho(x, y)$ is the density of the grid point at (x, y) . In SEMDOT, the threshold value Ψ is determined iteratively using the bi-section method such that the target volume constrain can be satisfied iteratively. Unlike the direct sensitivity-based level-set function presented by Da et al. [13] and Liu et al. [41], Equation 20 uses the densities of grid points that are determined originally based on sensitivity analysis (Equation 5). Therefore, Equation 20 can be regarded as an indirect sensitivity-based or grid point density based level-set function.

2.5. Convergence criteria

For BESO-based methods, the optimization procedure terminates when the average change of the objective function values in recent iterations is less than a prescribed tolerance value [68]. As previously mentioned by Sigmund and Maute [69], the convergence criterion of BESO could prematurely terminate the optimization procedure, because design variables may be in an oscillating state switching between 0 and 1 even though the objective function value based convergence criterion is satisfied. This oscillating state would result in a solution far from the optimum. On the other hand, the optimization procedure of standard SIMP is terminated when the maximum variation of design variables within two successive iterations is less than a prescribed tolerance [70]. However, when solving an optimization problem with a large number of elements, convergence difficulties can be observed in SIMP, as is discussed in Section 3.5.

If the Heaviside step function is considered in SEMDOT, the optimization procedure terminates when the overall topological alteration is less than its predefined tolerance value, which can be stated as:

$$\frac{\sum_{e=1}^M |X_e^k - X_e^{k-1}|}{\sum_{e=1}^M X_e^k} \leq \tau \quad (21)$$

where τ is the tolerance value for the overall topological alteration. This convergence criterion (Equation 21) is based on the overall measure of the variation of design variables compared to the local measure used in SIMP, and its better performance in determining convergency had been demonstrated by Fu et al. [43, 45, 46]. It is noted that Equation 21 can also be used in SIMP or BESO and is likely to improve their determination of termination point.

When the Heaviside smooth function is considered, intermediate elements that are not along the boundary will inevitably appear during the optimization process. Intermediate elements that are not along the boundary are the elements with the maximum grid point density less than 1 and the minimum density larger than ρ_{\min} . To measure the accuracy of the level-set function (Equation 20) representing the smooth topological boundary, an indicator termed topological boundary error is defined as the ratio of the number of the intermediate elements that are not along the boundary to the total number of elements. The topological boundary error convergence criterion is therefore stated as:

$$\frac{N_v}{M} \leq \epsilon; \quad (22)$$

where N_v is the number of intermediate elements that are not along boundaries, M is the total number of elements, and ϵ is the tolerance value for the topological boundary error. When the topological boundary error becomes negligible, intermediate elements are all distributed along the boundary, meaning that the level-set function accurately represents the current design.

In comparison to the Heaviside smooth function (Equation 16), the Heaviside step function (Equation 15) will not cause the topological boundary error, but it can cause numerical instabilities in SEMDOT, as is discussed in Section 3.1.

2.6. Optimization procedure

The optimization procedure of SEMDOT mainly consists of two parts: the implementation of structural changes based on elemental volume fractions and the generation of smooth topological boundaries based on the solid/void design of grid points. The improved and simplified flowchart of SEMDOT, which is based on the flowchart presented by Fu et al. [45], is illustrated in Figure 2.

3. Numerical Experiments

Benchmark 2D optimization problems are solved to demonstrate the validity of SEMDOT and exhibit the differences between SEMDOT and some existing algorithms: SIMP, BESO, and ETO. The prescribed value of the allowable volume V^* is set to 0.3. For all numerical examples, an isotropic linear elastic material model is assumed with Young's modulus of $E = 1$ MPa and Poisson's ratio of $\mu = 0.3$, and equally sized four-node plane-stress elements are used. Following the parametric studies in [46], $\beta_0 = 0.5$ and $\Lambda = 0.5$ are employed in the Heaviside smooth function (Equation 16), and the penalty coefficient of $p = 1.5$ is used in SEMDOT. The tolerance values of $\epsilon = 0.001$ and $\tau = 0.001$ are used in the convergence criteria. Following the parametric studies in [44], a grid with 10×10 points in each element is used. Unless otherwise stated, the heuristic filter radius Υ_{\min} is set to 1 time element width ($\Upsilon_{\min}=1$). In addition, the method of moving asymptotes (MMA) proposed by Svanberg [71] is used to update design variables, and default parameters in MMA are adopted.

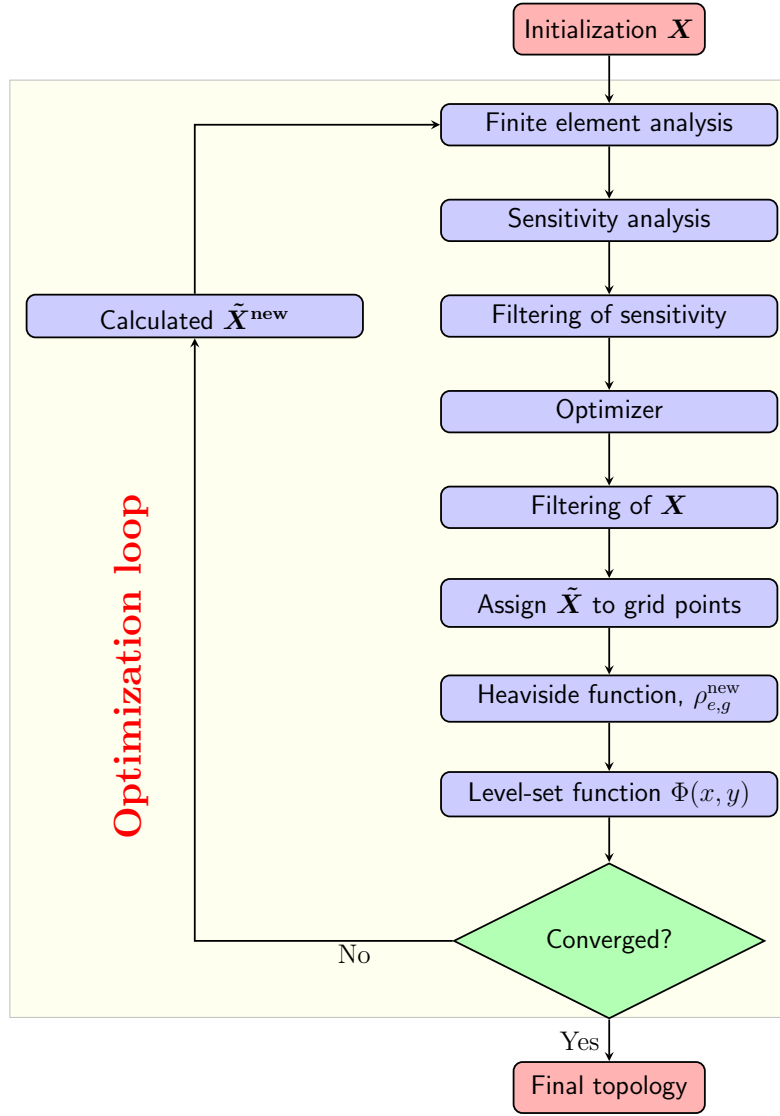


Figure 2: Flowchart of the SEMDOT method

3.1. Comparisons between Heaviside step and smooth functions

A simply supported deep beam subjected to a unit vertical load ($F = -1\text{N}$) at its bottom center is considered to investigate the influences of the Heaviside step and smooth functions on the topological design, performance, and convergency of SEMDOT. The design domain and boundary condition are shown in Figure 3. The bottom left corner is hinged, and the vertical displacement at the bottom right corner is prevented. A 180×90 mesh is used, and the filter radius r_{\min} is set to 2 time elements width ($r_{\min}=2$).

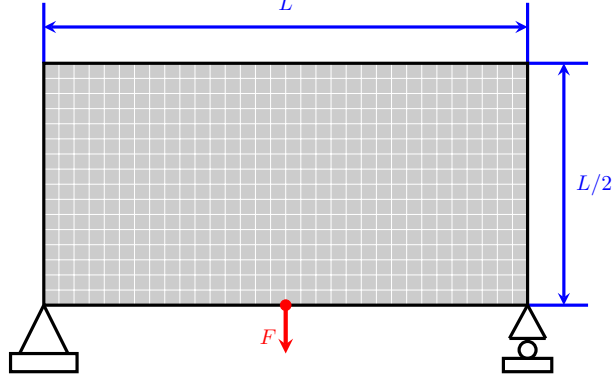


Figure 3: Design domain of a simply supported deep beam

The convergence history in Figure 4a shows that great fluctuations appear in the initial 20 iterations when the Heaviside step function is used. These fluctuations are associated with scattered material resulting in complicated topologies (Figures 4b and 4c), meaning that the Heaviside step function has the difficulty in extracting topological boundaries at the early stages of optimization. Afterwards, the optimization process steadily converges at 21.3875 J after 167 iterations and later topologies are reasonable (Figures 4d to 4g). Compared to the Heaviside step function, the Heaviside smooth function does not cause any numerical instabilities, and therefore the whole optimization process steadily converges at 21.1049 J after 142 iterations (Figure 5a). As shown in Figure 5a, the topological boundary error gradually decreases to almost 0% when the converged topology is obtained. Two different final topologies obtained by Heaviside step and smooth functions are shown in Figures 4g and 5b, respectively. In this case, the Heaviside smooth function performs better than the Heaviside step function both in compliance and convergence.

In some engineering problems, certain areas of the design domain are required to be void (non-design areas) during the whole optimization process. Another version of this problem with a non-designable circular hole with a radius of $L/6$ and a center located at $(L/2, L/4)$ as illustrated in Figure 6 is used to further test the performance of Heaviside step and smooth functions in SEMDOT. All parameter settings remain unchanged.

Figure 7a shows that SEMDOT using the Heaviside step function converges after 148 iterations, which is a little less than when the Heaviside smooth function is used (157). However, like the previous case, great fluctuations appear at the early stages of optimization when the Heaviside step function is used. Converged compliance is 23.6741 J for the Heaviside step function and 23.7306 J for the Heaviside smooth function, so the difference is negligible (around 0.2%). In this case, the Heaviside step function performs a little better than the Heaviside smooth function in compliance and convergence. However, the asymmetric topology obtained by the Heaviside step function has several tiny holes and one thin bar shown by a red circle in Figure 7b. This design cannot be easily manufactured even with AM [43]. By contrast, the symmetric topology obtained by the Heaviside smooth function has better manufacturability (Figure 7c).

Considering the symmetry condition in the case shown in Figure 6, comparisons of performance, convergency,

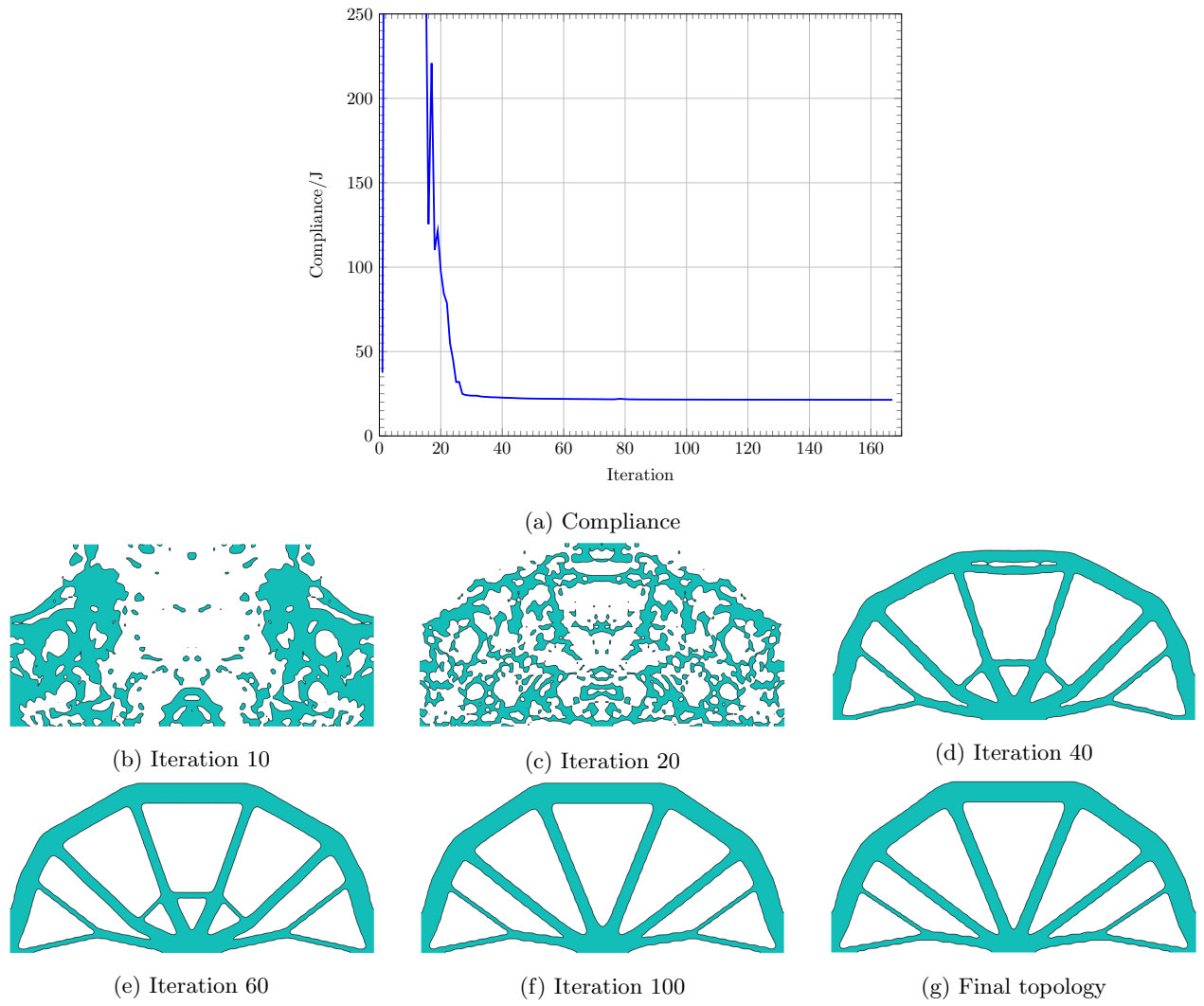


Figure 4: Compliance and optimized topology obtained with Heaviside step function for simply supported deep beam case

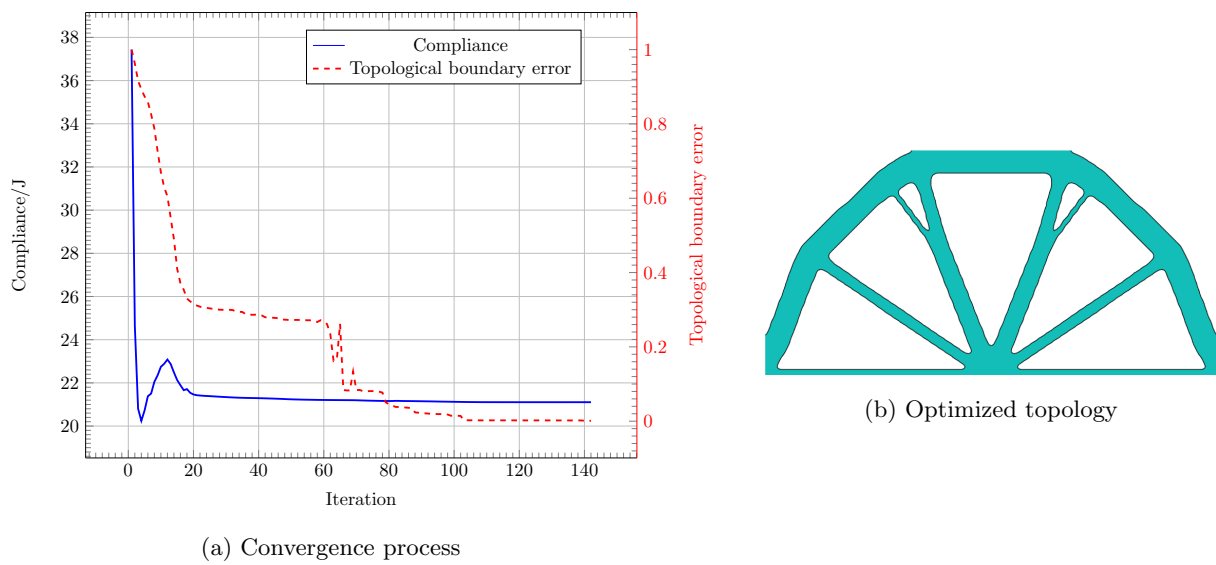


Figure 5: Convergence process and optimized topology obtained with Heaviside smooth function for simply supported deep beam case

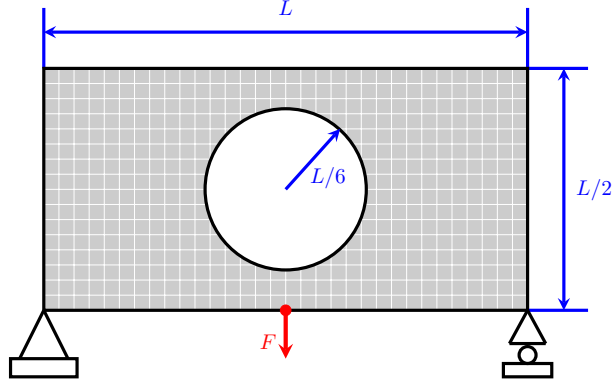
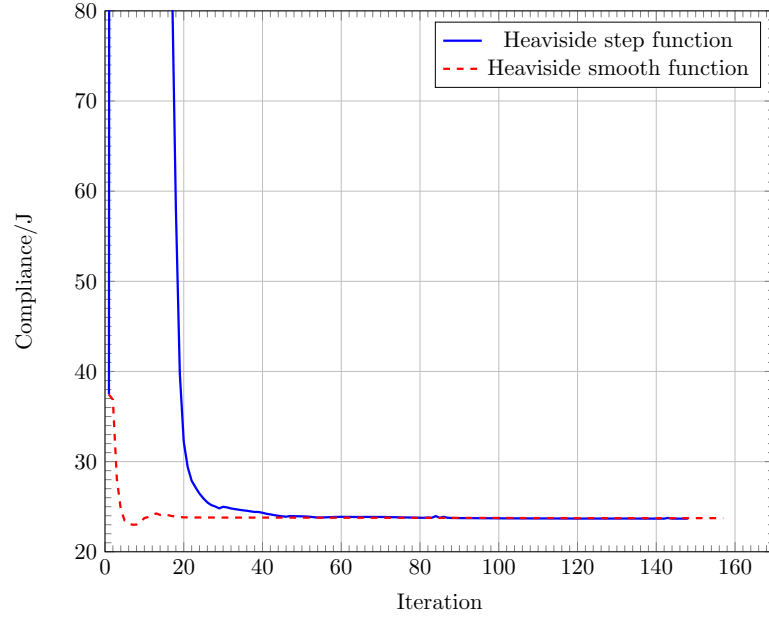
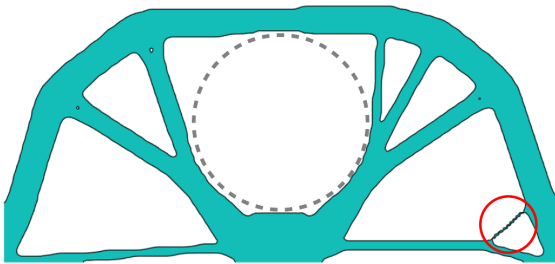


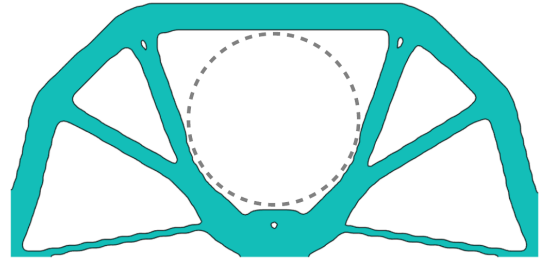
Figure 6: Design domain of a simply supported deep beam with a fixed hole



(a) Convergence histories



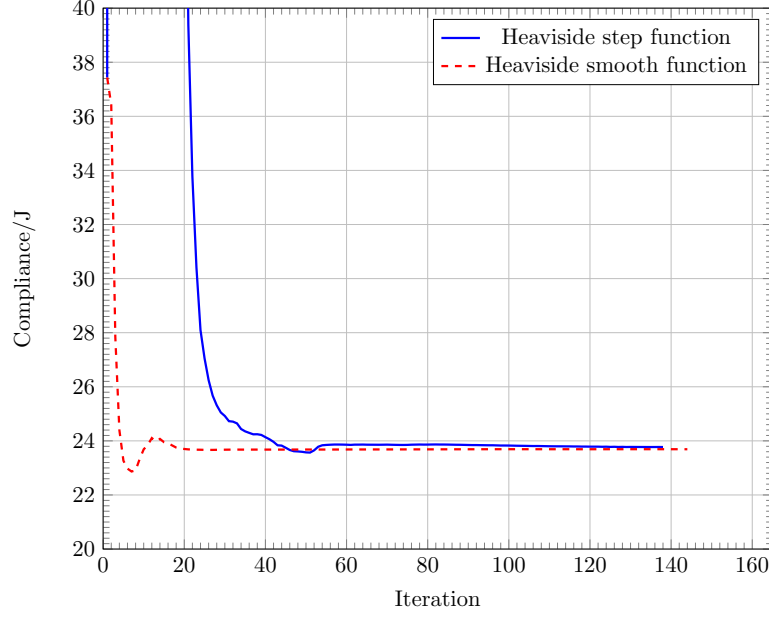
(b) Optimized topology obtained with Heaviside step function



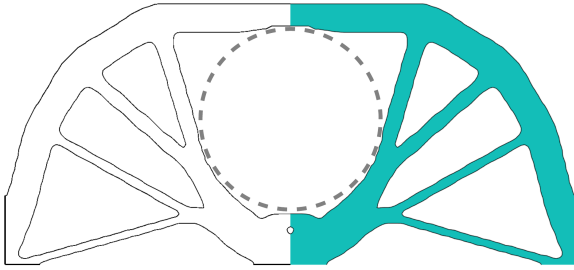
(c) Optimized topology obtained with Heaviside smooth function

Figure 7: Comparisons of performance, convergency, and topological designs between Heaviside step and smooth functions for simply supported deep beam case with a fixed hole

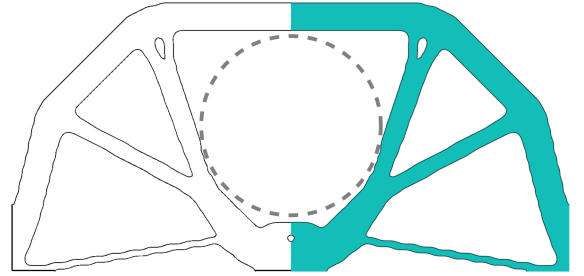
and topological designs between Heaviside step and smooth functions are shown in Figure 8. Identical to the previous discussion, the Heaviside smooth function needs a longer convergence process (157) than the Heaviside step function (138). Converged performance of the Heaviside smooth function (23.686 J) is slightly better than the Heaviside step function (23.772 J). In both cases, the performance changes before and after imposing symmetry are insignificant. In terms of topological designs, a clear difference can be observed between Figures 7b and 8b, but Figures 7c and 8c are almost identical. Therefore, it can be concluded that the Heaviside step function is more susceptible to the non-designable passive area compared to the Heaviside smooth function in SEMDOT. The asymmetric topology obtained by the Heaviside step function (Figure 7b) is because of the disturbance caused by the non-designable passive area during the determination of the topological boundary.



(a) Convergence histories



(b) Optimized topology obtained with Heaviside step function



(c) Optimized topology obtained with Heaviside smooth function

Figure 8: Comparisons of performance, convergency, and topological designs between Heaviside step and smooth functions considering symmetry condition

Based on the above discussions, it is concluded that the Heaviside smooth function is more suitable than the Heaviside step function for SEMDOT despite requiring an additional termination criterion (Equation 22). Therefore, the Heaviside smooth function will be used for the rest of numerical experiments in this paper rather than the Heaviside step function.

3.2. Deviation of filtered elemental volume fractions

Following Section 3.1, a coarse mesh of 20×20 is used for the simply supported deep beam case considering both the passive area and symmetry condition to demonstrate the relationship between \tilde{X}_e and \tilde{X}_e^{new} (Equation 19). In this case, the filter radius r_{\min} is set to 1.5 time elements width ($r_{\min}=1.5$). The optimized topology with element numbers is shown in Figure 9. The histogram of the difference between \tilde{X}_e and \tilde{X}_e^{new} (δ_e) for the final topology is shown in Figure 10, which reveals that the deviation δ_e mainly concentrates on the range from -0.2 to 0.2, and there is no difference between \tilde{X}_e and \tilde{X}_e^{new} for the majority of elements ($\delta_e=0$).

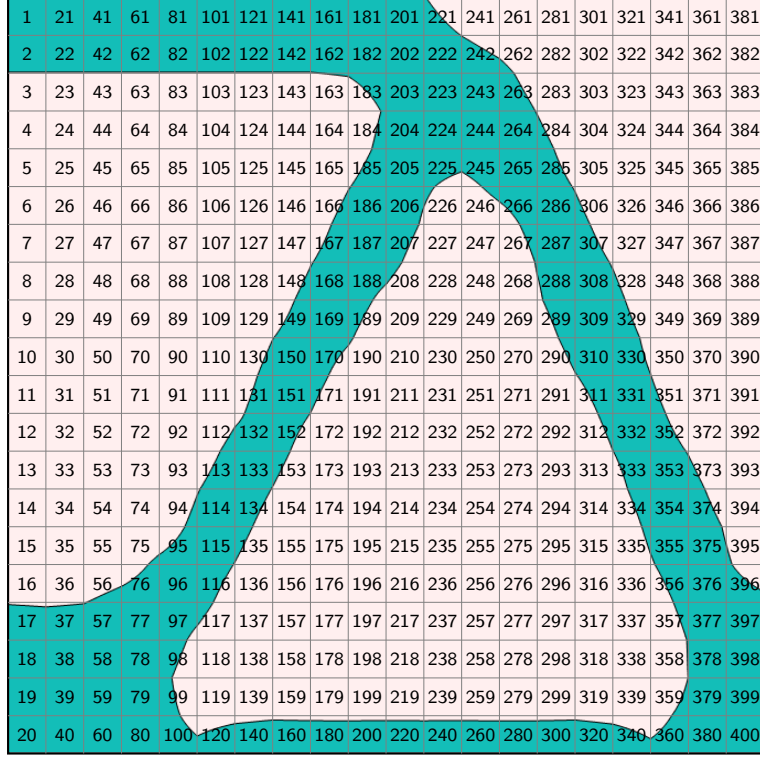


Figure 9: Optimized topology with element numbers

To explain the relationship between \tilde{X}_e and \tilde{X}_e^{new} in each iteration, values of \tilde{X}_e and \tilde{X}_e^{new} for elements 16, 79, 195, 202, 247, and 360 are shown in Figure 11. The biggest difference ($\delta_e=-0.8142$ in the final iteration) appears in element 16, as illustrated in Figure 11a. Even though element 16 has a relatively high value of \tilde{X}_e during the optimization process, its \tilde{X}_e^{new} goes down to 0.001. This is because element 16 is in the passive area, meaning that it needs to be artificially suppressed to the void element. For the rest of elements that are not in the passive area, \tilde{X}_e^{new} is approximately proportional to \tilde{X}_e , as illustrated in Figures 11b, 11c, 11d, 11e, and 11f. The function of Equation 9 is to filter elemental volume fractions X_e without considering the target volume constraint, so there is $\sum_{e=1}^M \tilde{X}_e/V = 0.3125 > V^*/V$ in the final iteration. Therefore, the use of \tilde{X}_e for the next round of FEA will result in the overestimation of structural performance at least in this case. By contrast, \tilde{X}_e^{new} is calculated from the newly obtained grid point densities that are determined based on the target volume constraint (refer to Equations 16 and 18), so $\sum_{e=1}^M \tilde{X}_e^{new}/V = 0.3 = V^*/V$ can be guaranteed iteratively.

When the passive area is not considered in the test case, there is no big deviation such as the one observed in element 16 (Figure 11a), and the deviation δ_e mainly falls in the range of -0.2 to 0.2 (Figure 12).

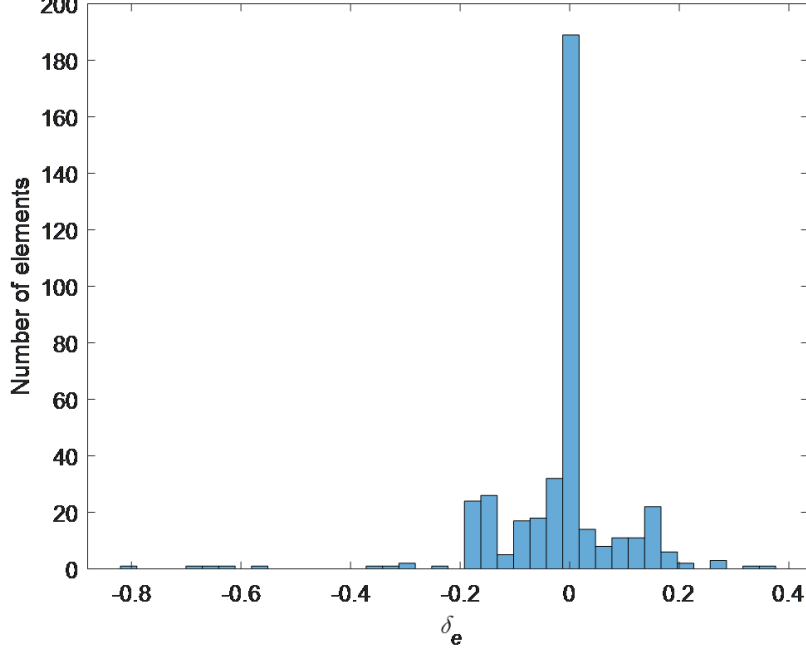


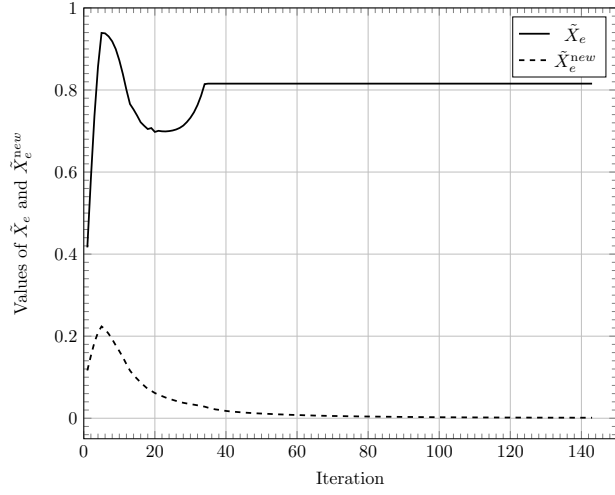
Figure 10: Histogram of δ_e with passive area

3.3. Effects of multiple filtering steps

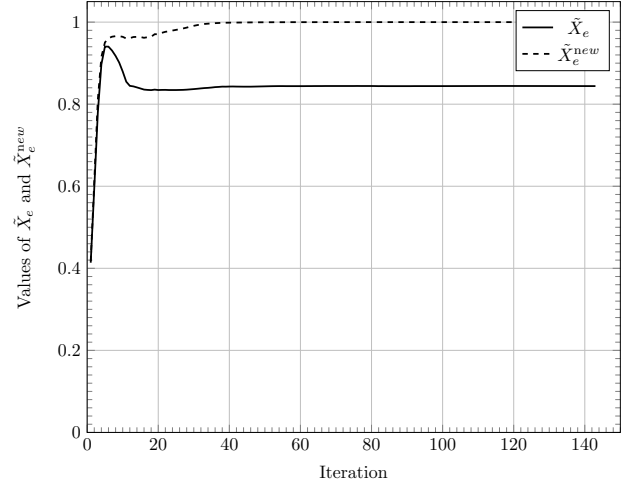
Two combinations of filter radii (i.e., $r_{\min} = 3$, $\Upsilon_{\min} = 3$ and $r_{\min} = 3$, $\Upsilon_{\min} = 1$) were used in authors' previous works [43, 44, 45, 46]. Other than those two combinations, different combinations of filter radii can also be considered in optimizing topologies with SEMDOT, which provides more design freedom for designers. The so-called MesserschmidtBlkowBlohm (MBB) beam is used here to demonstrate the effects of the two filter radii, r_{\min} and Υ_{\min} , on performance, convergency, and topological designs. The design domain and boundary conditions are shown in Figure 13. Only half of the MBB beam is considered as the design domain due to symmetry. As illustrated in Figure 13, the symmetric boundary condition is applied to the left side; the vertical displacement at the bottom right corner is restricted; and a unit vertical load ($F=-1$ N) is applied at the top left corner. The design domain is discretized by a 150×50 finite element mesh.

Figure 14a shows that the highest compliance (287.2474 J) is obtained when the combination of $r_{\min} = 1$ and $\Upsilon_{\min} = 2.8$ is used. This drops to 283.7538 J when the combination of $r_{\min} = 2.8$ and $\Upsilon_{\min} = 1$ is used, meaning that Υ_{\min} will cause worse results than r_{\min} . Generally, increasing either r_{\min} or Υ_{\min} can contribute to the rise of compliance, and then a relatively stable value can be reached when either r_{\min} or Υ_{\min} is large enough. Figure 14b shows that using high values of Υ_{\min} will prolong the convergence process more than using high values of r_{\min} , and the highest number of iterations (378) is obtained when $r_{\min} = 2.6$ and $\Upsilon_{\min} = 3$.

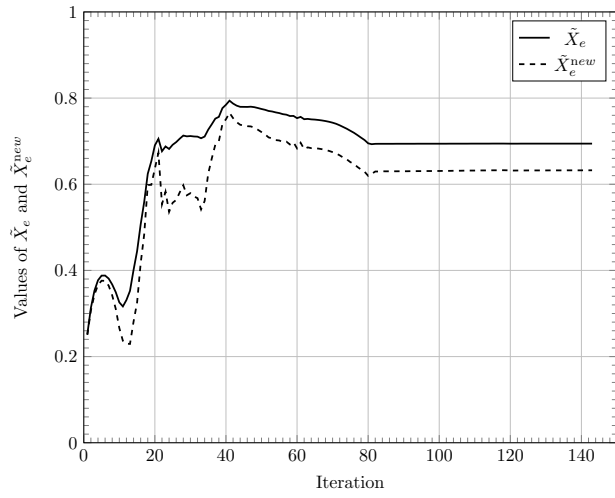
Topological designs with different combinations of r_{\min} and Υ_{\min} are shown in Figure 15. Length scales representing r_{\min} and Υ_{\min} are added into Figure 15 as reference. Increasing either r_{\min} or Υ_{\min} results in simpler topologies with less holes. Small holes vanish when the combination of $r_{\min} = 3$ and $\Upsilon_{\min} = 3$ is used, which is beneficial to the manufacturability of optimized topologies. Figure 16 shows the compliance, convergence, and topological designs under large values of r_{\min} and $\Upsilon_{\min}=1$. As topological designs from $r_{\min} = 3.5$ have the similar structural layout with no small holes, only the topology at $r_{\min} = 3.5$ and $\Upsilon_{\min}=1$ is given in Figure 16 for simplicity. Compliance and the number of iterations of the combination of $r_{\min} = 3.5$ and $\Upsilon_{\min} = 1$ are 284.3535 J and 274, respectively, which are close to those of the combination of $r_{\min} = 3$ and $\Upsilon_{\min} = 3$ (284.2814 J and 290,



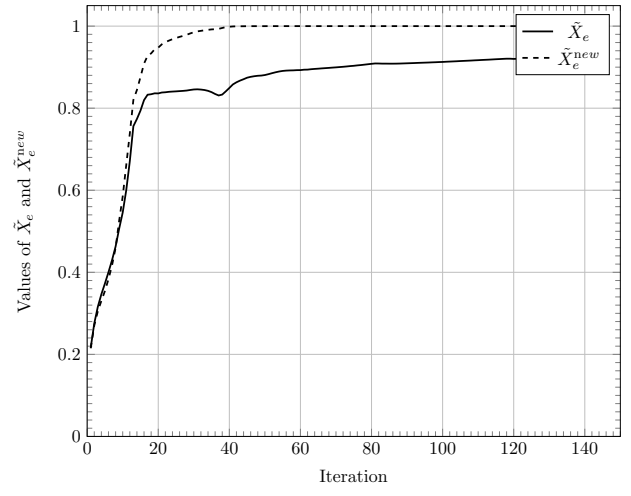
(a) Element 16



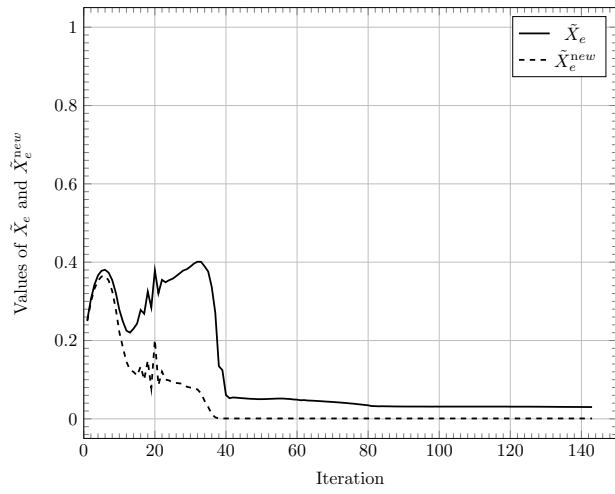
(b) Element 79



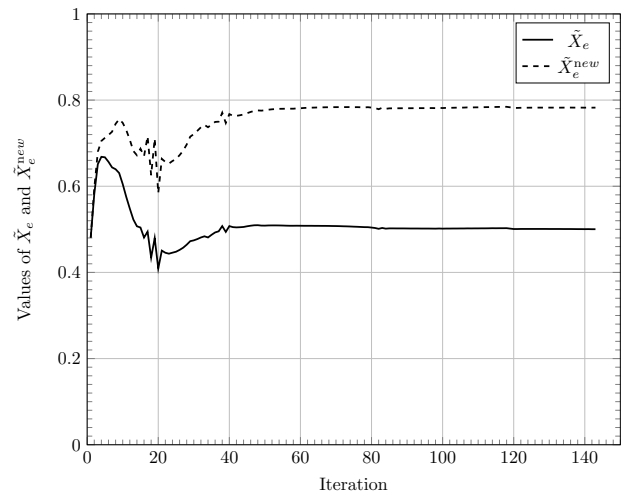
(c) Element 185



(d) Element 202



(e) Element 247



(f) Element 360

Figure 11: Values of \tilde{X}_e and \tilde{X}_e^{new} for different elements

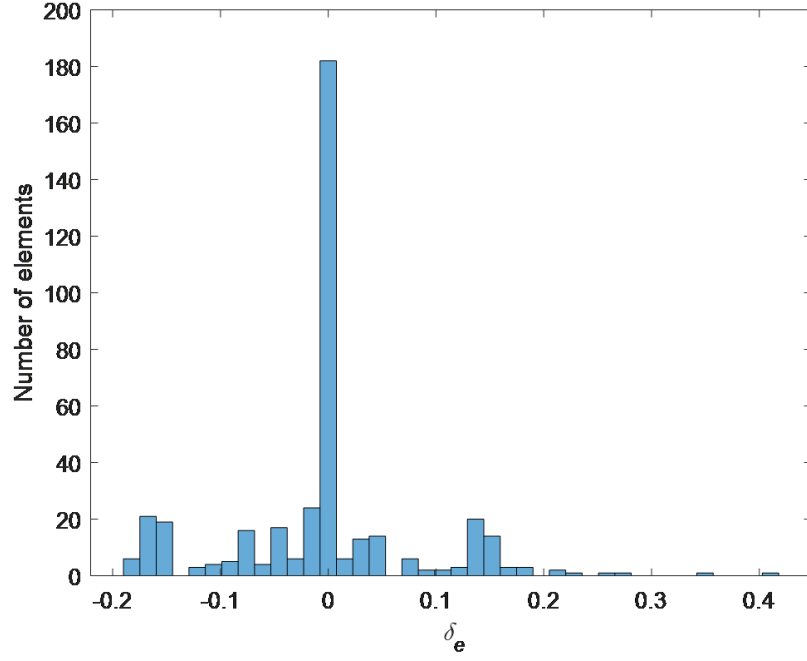


Figure 12: Histogram of δ_e without passive area

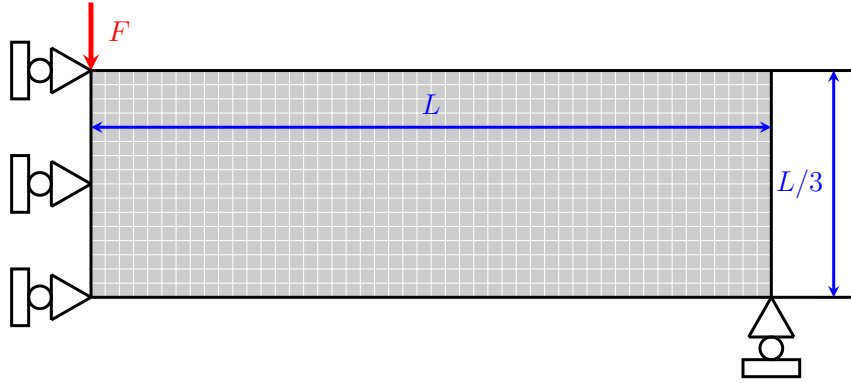


Figure 13: Design domain of half an MBB beam

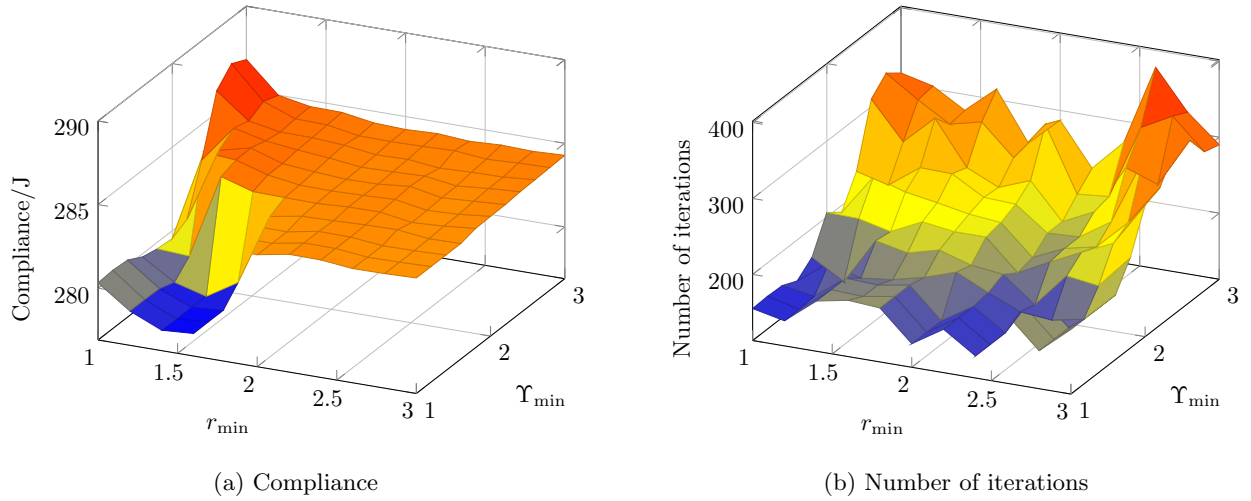


Figure 14: Compliance and number of iterations for different values of r_{\min} and Υ_{\min} solving MBB beam case

respectively). There is an overall tendency for compliance to increase with r_{\min} (Figure 16). When r_{\min} reaches 3.9 and 4, large numbers of iterations (627 and 606, respectively) are required to reach convergence, as shown in Figure 16.

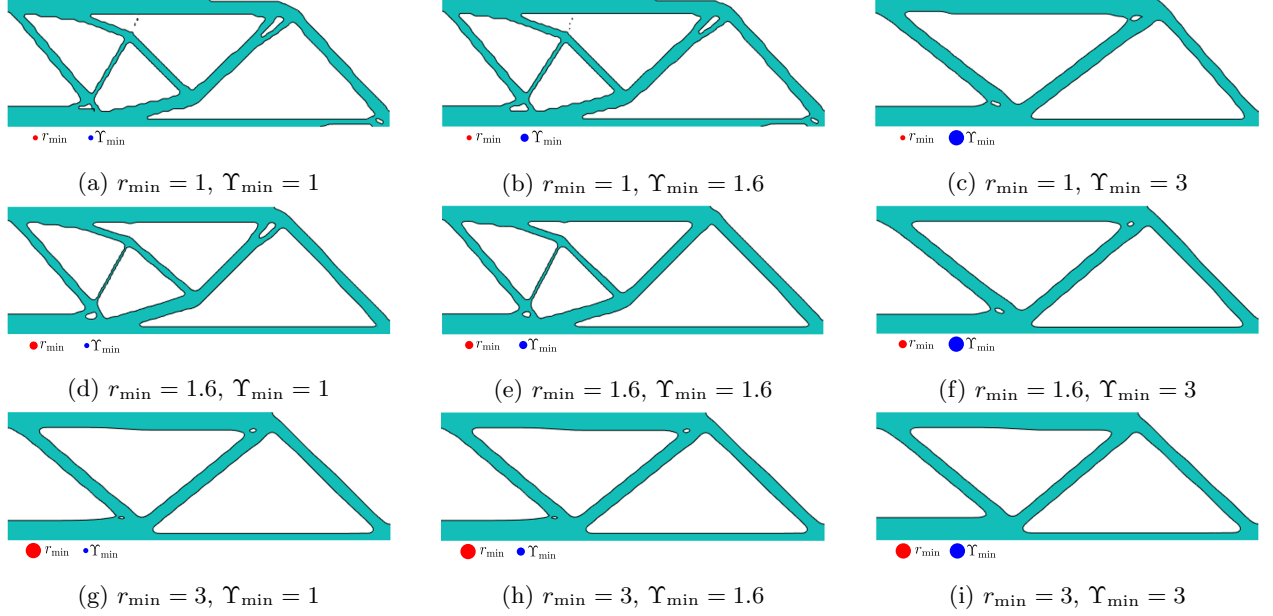


Figure 15: Optimized topologies with different combinations of r_{\min} and Υ_{\min} for MBB beam case

Even though Equation 9 is basically used for filtering elemental volume fractions in SEMDOT, and the main function of Equation 12 is to assign elemental volume fractions to grid points, different combinations of r_{\min} and Υ_{\min} can also be considered in SEMDOT to explore different topological designs with better performance, quick convergence, or both. Generally, the fixed value of $\Upsilon_{\min}=1$ is recommended for the convenience of implementation.

3.4. Validation of sensitivity analysis method

To further validate the effectiveness of the sensitivity analysis method (Equation 5), one typical compliant mechanism design problem (Figure 17) is considered. The input force F_{in} is set to 1 N, and input (k_{in}) and output (k_{out}) spring stiffnesses are set to 1 and 0.001, respectively. The design domain is discretized by a 80×40 finite element mesh, and the filter radius r_{\min} is set to 2 time elements width ($r_{\min}=2$).

The optimization process converges at the output displacement of 1.0197 mm after 116 iterations (Figure 18a), and the correct topological design is obtained by SEMDOT (Figure 18b). Based on the results in Figure 18, it can be concluded that the sensitivity analysis method adopted in SEMDOT is suitable for compliant mechanism design, which is more challenging than compliance minimization design. The effectiveness of the sensitivity analysis method in SEMDOT is therefore proved.

3.5. Numerical comparisons

Cantilever beam and L-bracket beam test cases are used to thoroughly compare SEMDOT with some well-established element-based algorithms in the ability of seeking the optimal solution and convergency. Only methods with published source codes (i.e., SIMP [72], BESO [73], and ETO [13]) are selected in this comparison, together with SEMDOT with the single filtering step (Equation 12). In terms of SIMP, two typical filters: the density filter [74, 75, 62] and the Heaviside projection filter [64] are considered. In the Heaviside projection filter, the parameter controlling the smoothness of the approximation is gradually increased from 1 to 128 by doubling its value every

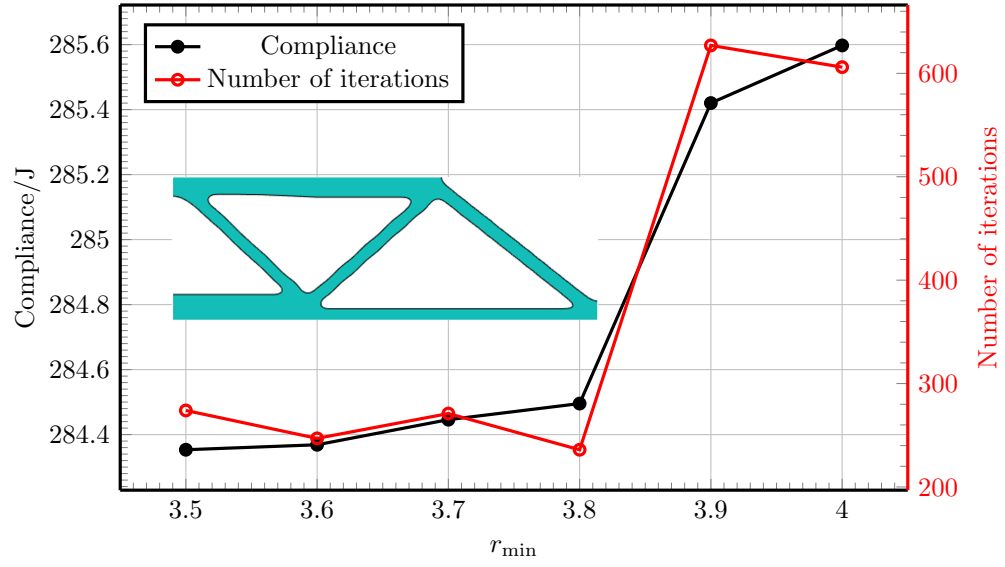


Figure 16: Compliance, convergence, and topological designs under large values of r_{\min} and $\Upsilon_{\min}=1$

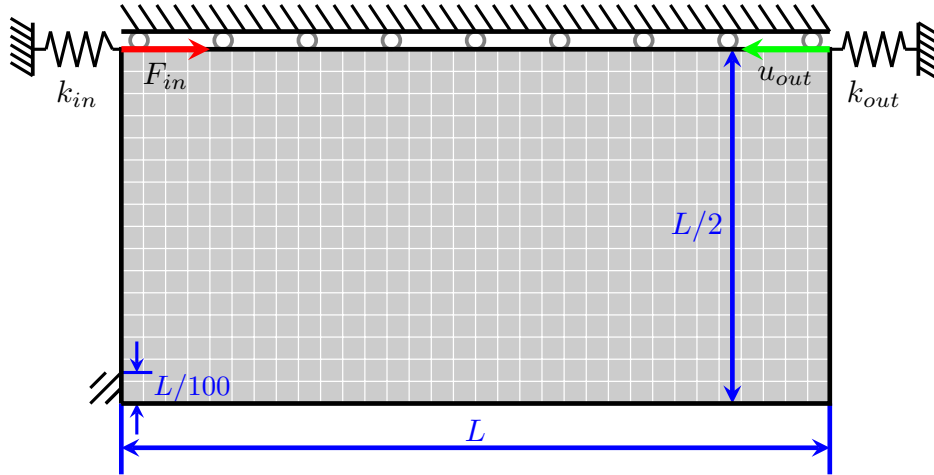


Figure 17: Force inverter design problem

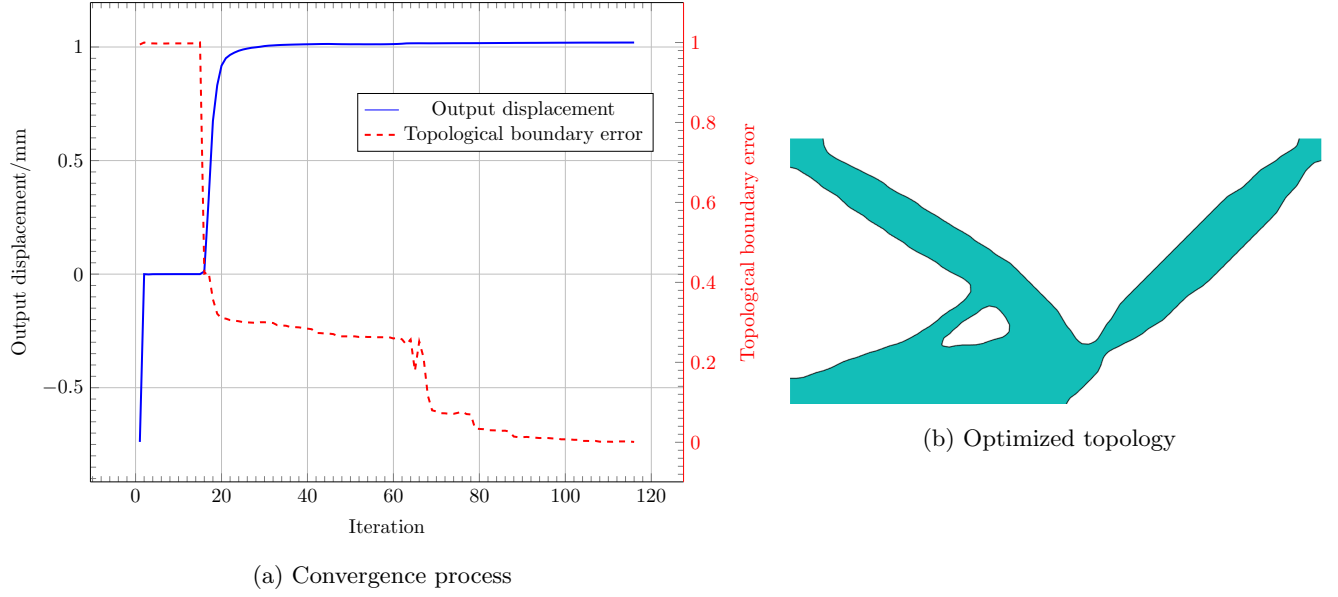


Figure 18: Convergence process and optimized topology for force inverter design case

25 iterations or when the change between two consecutive designs is less than 0.01. For simplicity, SIMP-D and SIMP-H are used to represent SIMP with density and Heaviside projection filters, respectively, in graph legends and captions. In addition, SEMDOT-S is used to represent SEMDOT with the sole heuristic filter in graph legends and captions. The penalty coefficient of 1.5 is used in SEMDOT, SEMDOT-S, and ETO, and the penalty coefficient of 3 is used in SIMP and BESO. For BESO and ETO, the evolution rate er is set to 2%. In addition, the maximum number of iterations is set to 300 for all methods.

The design domain and boundary condition of a deep cantilever beam are shown in Figure 19. The left side is fixed and a unit vertical load ($F = -1\text{N}$) is imposed at the center point of the right side. The design domain of this beam is discretized by a 150×100 finite element mesh. The filter radius r_{\min} is set to 2.5 time elements width ($r_{\min}=2.5$).

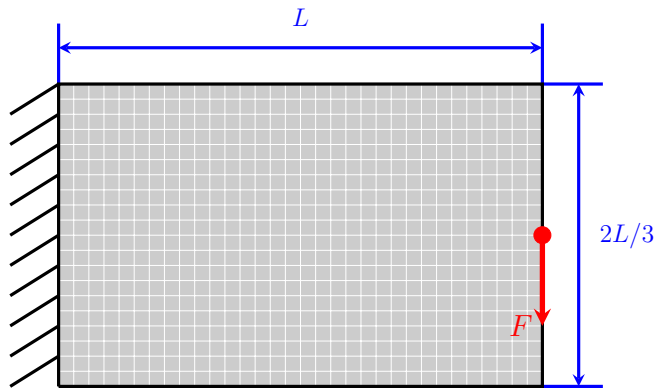


Figure 19: Design domain of a deep cantilever beam

Figure 20a shows that the best compliance (49.6856 J) is obtained by ETO, followed by 51.1240 J obtained by SEMDOT. The optimization process of ETO converges after 95 iterations, which is less than that of SEMDOT (123 iterations). SEMDOT-S converges at the compliance of 51.1558 J after 124 iterations, which is almost identical to SEMDOT, whereas two different topological designs are obtained (Figures 20b and 20c). Even though both

SEMDOT and ETO are based on elemental volume fractions, optimized topologies (Figures 20b and 20g) are different. The topological design obtained by SEMDOT is similar to those obtained by SIMP (Figures 20d and 20e), and the topological design obtained by ETO is similar to that of BESO (Figure 20f). In this case, ETO is superior to SEMDOT in performance and convergence. The worst compliance (60.0841 J) is obtained by SIMP with the density filter. This is because intermediate elements are allowed to distribute across the whole design domain, and intermediate elements result in smaller improvement of stiffness per density due to the use of penalty factor. BESO converges at the compliance of 51.7538 J after 69 iterations, which is better than SIMP with the Heaviside projection filter with $C=53.3355$ J after 204 iterations.

Effects of different mesh sizes and domain aspect ratios are considered to provide statistical comparisons. As the element size is scaled with a certain ratio for test cases with different mesh sizes, the filter radius is scaled with the same ratio to ensure that its absolute value remains constant. Table 1 demonstrates that performance obtained by ETO is still the best for different mesh sizes. Performance obtained by SEMDOT-S is the second best for the mesh sizes ranging from 60×40 to 120×80 , and performance obtained by SEMDOT is the second best for the mesh sizes ranging from 180×120 to 270×180 . Table 2 demonstrates that BESO converges the fastest for different mesh sizes, followed by ETO. SEMDOT-S performs better than SEMDOT in terms of convergency. Both SIMP-D and SIMP-H face the convergence difficulty when the fine mesh is used.

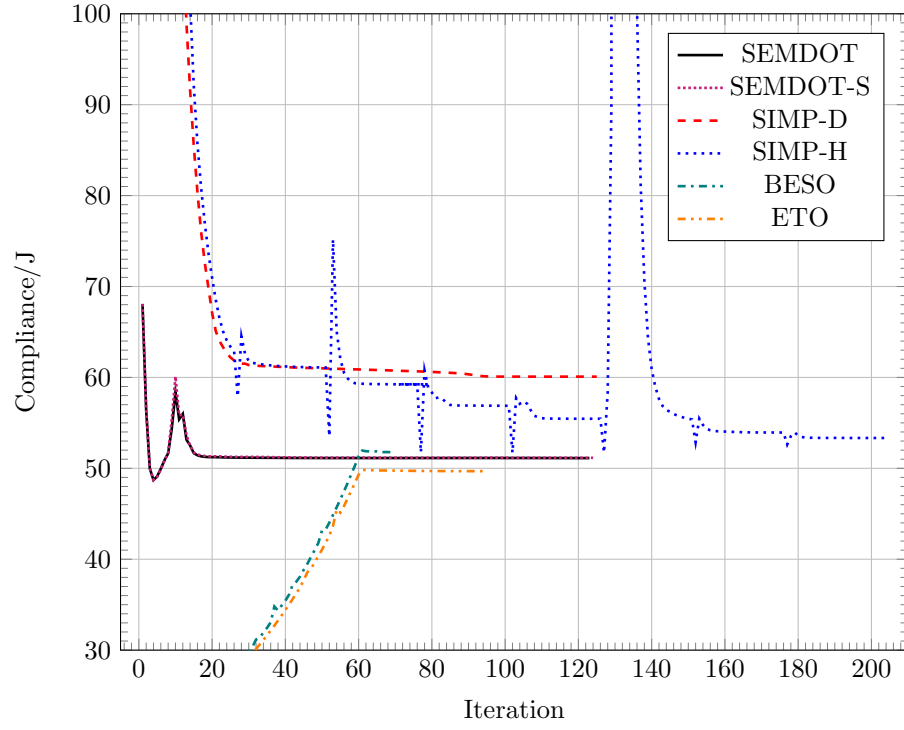
Table 1: Effects of mesh size on compliance obtained by different algorithms solving deep cantilever beam case

Algorithms	Mesh size						
	60×40	90×60	120×80	180×120	210×140	240×160	270×180
SEMDOT	51.0698	50.9852	50.9763	51.2065	51.2797	51.3474	51.3796
SEMDOT-S	51.0698	50.9200	50.9716	51.3621	51.5000	51.5254	51.6761
SIMP-D	65.6168	59.8601	59.0882	59.7609	60.1124	60.1080	60.2780
SIMP-H	61.9331	52.6167	205.9870	54.1442	53.4234	65.8000	64.4706
BESO	55.0152	52.7312	51.8462	51.2688	51.2836	51.3759	51.2489
ETO	49.6404	49.2007	49.6575	49.8537	49.9187	50.0130	50.0750

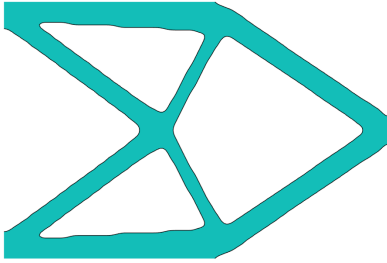
Table 2: Effects of mesh size on number of iterations obtained by different algorithms solving deep cantilever beam case

Algorithms	Mesh size						
	60×40	90×60	120×80	180×120	210×140	240×160	270×180
SEMDOT	128	93	104	138	158	179	197
SEMDOT-S	128	79	165	132	152	173	196
SIMP-D	36	98	102	215	300	300	300
SIMP-H	130	199	198	277	256	300	300
BESO	70	70	69	81	70	70	70
ETO	78	99	97	86	93	94	99

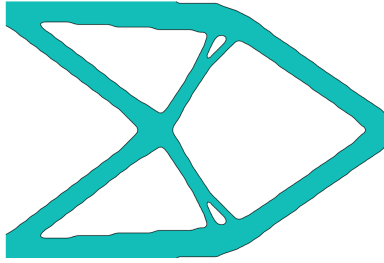
In terms of different domain aspect ratios, the number of elements in the vertical direction is fixed at 60, and the filter radius r_{\min} is set to 1.5 time elements width ($r_{\min}=1.5$). Table 3 demonstrates that ETO obtains better performance than both SEMDOT and SEMDOT-S. Performance obtained by SEMDOT-S is the second best for



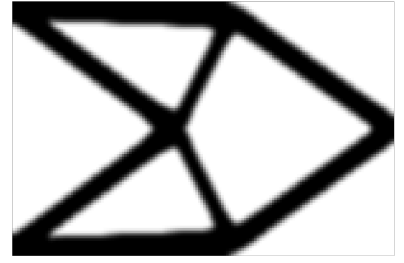
(a) Convergence histories



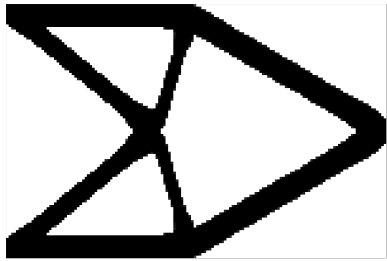
(b) SEMDOT



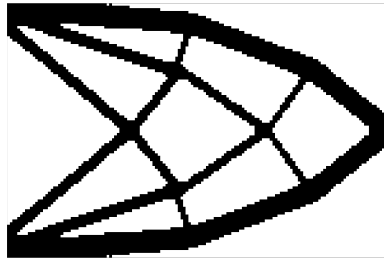
(c) SEMDOT-S



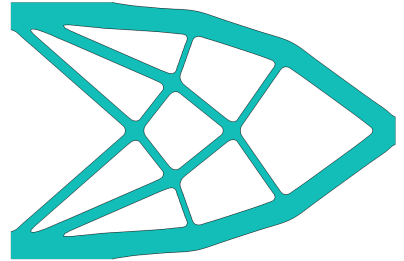
(d) SIMP-D



(e) SIMP-H



(f) BESO



(g) ETO

Figure 20: Comparisons of performance, convergence, and topological designs between different algorithms for deep cantilever beam case

the domain aspect ratios of 0.5:1, 1:1, and 2.5:1, and performance obtained by SEMDOT is the second best for the domain aspect ratios of 2:1 and 3:1. Table 4 demonstrates that SEMDOT converges faster than ETO for the domain aspect ratios of 2.5:1 and 3:1, and SEMDOT-S converges faster than ETO for the domain aspect ratios of 0.5:1, 1:1, 2.5:1, and 3:1.

Table 3: Effects of domain aspect ratio on compliance obtained by different algorithms solving deep cantilever beam case

Algorithms	Domain aspect ratio				
	0.5:1	1:1	2:1	2.5:1	3:1
SEMDOT	7.8023	22.0224	94.7833	159.2461	248.6884
SEMDOT-S	7.7981	21.9979	95.0301	159.1104	250.2365
SIMP-D	8.7245	25.7240	108.7384	187.2112	292.0282
SIMP-H	7.9776	23.1224	98.0371	302.8705	260.9999
BESO	7.8691	22.9724	98.6805	168.8078	259.6505
ETO	7.7621	21.7892	94.7019	159.2034	246.9935

Table 4: Effects of domain aspect ratio on number of iterations obtained by different algorithms solving deep cantilever beam case

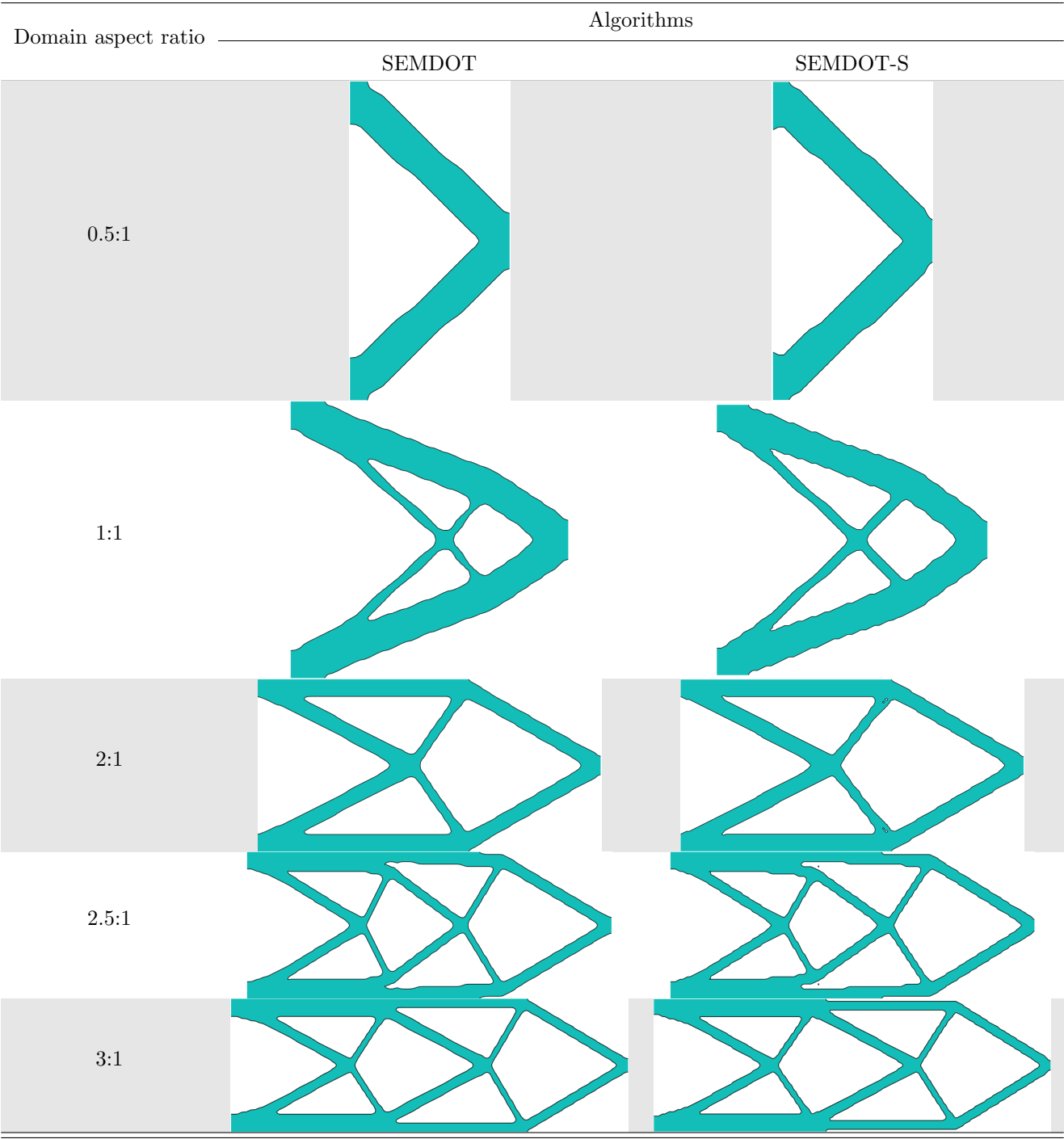
Algorithms	Domain aspect ratio				
	0.5:1	1:1	2:1	2.5:1	3:1
SEMDOT	91	158	125	126	110
SEMDOT-S	66	88	112	84	91
SIMP-D	35	93	135	160	144
SIMP-H	207	206	208	257	225
BESO	69	70	74	64	86
ETO	75	95	98	171	180

Even though SEMDOT-S performs better than SEMDOT for some test cases, it cannot be concluded that the use of multiple filtering step is not needed. This is because the rationality of obtained topologies is also an important assessment criteria. Table 5 gives the comparisons of topological designs obtained by SEMDOT and SEMDOT-S for deep cantilever beam cases considering different domain aspect ratios. The topological boundary obtained by SEMDOT is smoother than SEMDOT-S for the test case with the domain aspect ratio of 1:1. SEMDOT-S forms tiny holes when the domain aspect ratio is 2:1 and discontinuous structures when the domain aspect ratio is 2.5:1. By contrast, SEMDOT does not generate such structural features.

The second test case is an L-bracket, for which the design domain and boundary condition are shown in Figure 21. Here L is set to 400 element width. The top edge is fixed, and a unit vertical load ($F = -1\text{N}$) is applied at the top corner of the right side. The filter radius r_{\min} is set to 4 time elements width ($r_{\min}=4$).

In this example, the best compliance (228.9422 J) is obtained by SEMDOT, followed by 232.9864 J obtained by SEMDOT-S (Figure 22a). The optimization process of ETO converges at the compliance of 249.2654 J after 79 iterations where its number of iterations is still less than those of SEMDOT (181 iterations) and SEMDOT-S (243 iterations). Both SIMP algorithms face difficulties in convergence when the fine mesh is used, so optimization processes terminate after reaching the preset maximum number of iterations (300). By contrast, optimization

Table 5: Comparisons of topologies with different domain aspect ratios between SEMDOT and SEMDOT-S for deep cantilever beam case



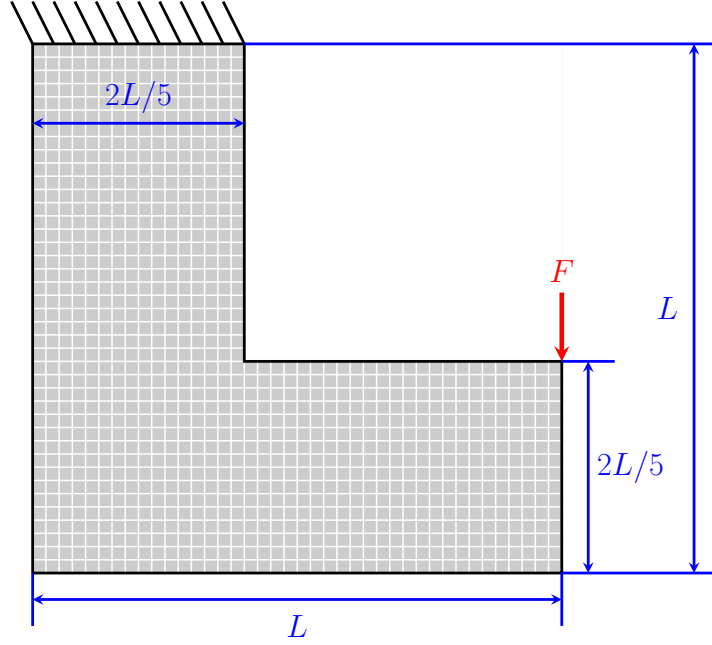


Figure 21: Design domain of an L-bracket beam

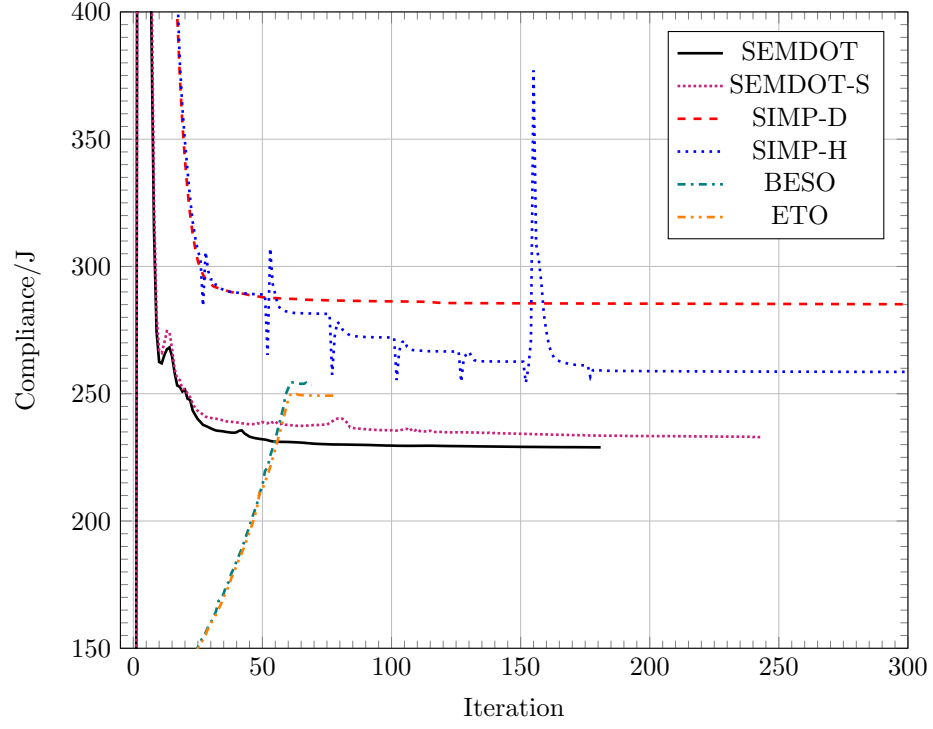
processes of SEMDOT, SEMDOT-S, BESO, and ETO converge within 250 iterations. Interestingly, as is evident from Figure 22a, numerical instabilities occur in the initial 10 iterations of the optimization processes of SEMDOT and SEMDOT-S despite using the Heaviside smooth function. This is because of the joint effects of the non-designable passive area and specific load and boundary conditions. Afterwards, the optimization process quickly settles to a steady pass. Unlike SEMDOT and SIMP (Figures 22b, 22d, and 22e), SEMDOT-S, BESO, and ETO are prone to resulting in topological designs with thin features (Figures 22c, 22f, and 22g), which are not preferred from the manufacturing point of view despite using the same value for the filter radius.

Effects of different mesh sizes and domain aspect ratios are also investigated for the L-bracket beam case. Table 6 demonstrates that performance obtained by SEMDOT is the best for the majority of test cases with different mesh sizes, followed by SEMDOT-S. ETO ranks the third position in terms of performance. Table 7 demonstrates that BESO converges the fastest for different mesh sizes, followed by ETO. SEMDOT performs better than SEMDOT-S in the aspect of convergency for most of cases.

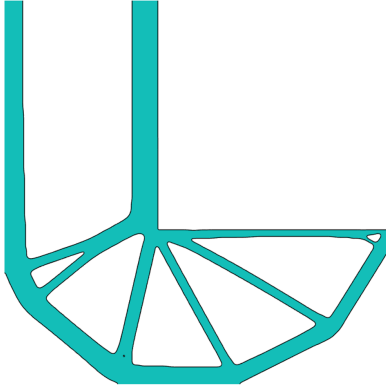
Table 6: Effects of mesh size on compliance obtained by different algorithms solving L-bracket beam case

Algorithms	Mesh size				
	$L=150$	$L=200$	$L=250$	$L=300$	$L=350$
SEMDOT	225.8848	225.4980	229.3275	228.3329	229.5550
SEMDOT-S	225.9183	232.6018	229.7667	231.2625	229.9703
SIMP-D	289.0603	281.0499	286.5398	285.2692	286.9609
SIMP-H	256.3416	255.9985	261.8570	267.4361	263.0003
BESO	257.7212	257.4816	256.4764	254.6842	253.9468
ETO	245.8689	247.1456	248.7580	248.4174	249.1365

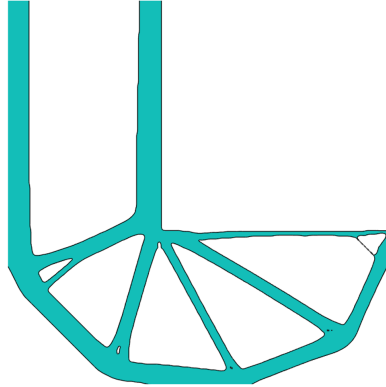
To further demonstrate the difference between SEMDOT and SEMDOT-S, topological designs obtained by



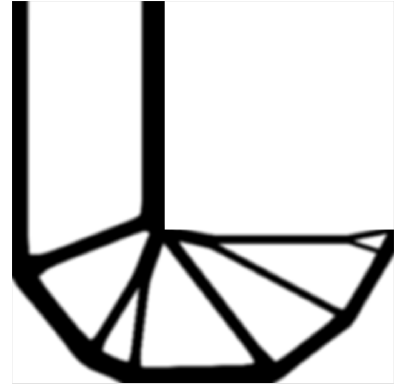
(a) Convergence histories



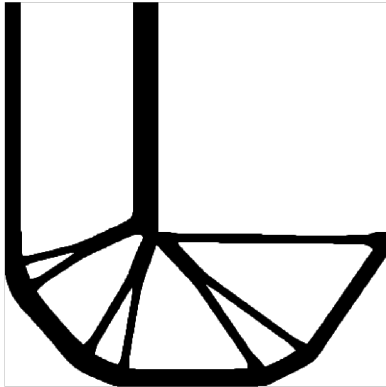
(b) SEMDOT



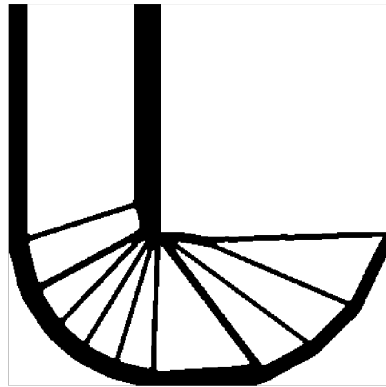
(c) SEMDOT-S



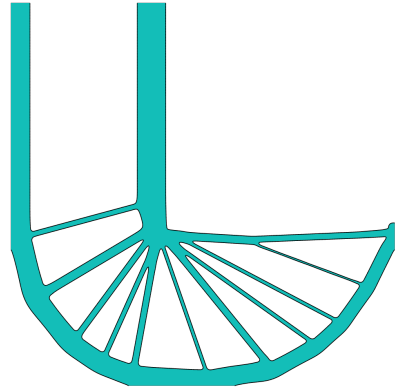
(d) SIMP-D



(e) SIMP-H



(f) BESO



(g) ETO

Figure 22: Comparisons of performance, convergence, and topological designs between different algorithms for L-bracket beam

Table 7: Effects of mesh size on number of iterations obtained by different algorithms solving L-bracket beam case

Algorithms	Mesh size				
	$L=150$	$L=200$	$L=250$	$L=300$	$L=350$
SEMDOT	169	245	198	211	224
SEMDOT-S	204	282	208	300	208
SIMP-D	300	300	300	300	300
SIMP-H	248	205	212	300	300
BESO	68	69	70	74	72
ETO	86	81	119	82	85

SEMDOT and SEMDOT-S for the test cases considering different mesh sizes are listed in Table 8. Similar with the cantilever beam case, SEMDOT-S forms thin features when mesh sizes are $L=250$ and $L=300$, and discontinuous structures when mesh sizes are $L=150$ and $L=350$. The mentioned structural features are not observed in the topological designs obtained by SEMDOT.

In terms of different domain aspect ratios, the number of elements in the vertical direction is fixed at 200, and the filter radius r_{\min} is set to 2 time elements width ($r_{\min}=2$). Table 9 demonstrates that performance obtained by SEMDOT and SEMDOT-S is better than ETO, and SEMDOT generally obtains better or comparable performance compared to SEMDOT-S. Table 10 demonstrates that SEMDOT performs better than SEMDOT-S in terms of convergency for most of test cases, and BESO and ETO generally converge faster than other algorithms.

Although BESO shows the fastest convergency in these two test cases, this may be because of the premature termination mentioned in Section 2.5, and the same issue seems to occur in ETO because of using the same termination criterion. Otherwise, BESO and ETO could have the potential to obtain better performance. ETO converges slower than BESO as it uses elemental volume fractions in the FEA model instead of elemental densities. On the contrary, SEMDOT converges faster than SIMP because of distributing intermediate elements only along boundaries and introducing new termination criteria (Equations 21 and 22). Based on the above discussion, SEMDOT-S easily obtains thin features and discontinuous structures, and performance obtained by SEMDOT-S is generally worse than SEMDOT for test cases with the fine mesh (refer to Tables 1, 3, 6, and 9). Therefore, it can be concluded that the use of multiple filtering steps is more suitable than single filtering step in SEMDOT.

4. Conclusions

This paper explains the algorithm mechanism of SEMDOT using several numerical examples. Performance of SEMDOT is demonstrated through numerical comparisons with a range of well-established element-based algorithms. Concluding remarks can be stated as follows:

- The Heaviside smooth function is more suitable than the Heaviside step function for SEMDOT to obtain a more robust algorithm.
- The use of multiple filtering steps enhances the flexibility of SEMDOT in exploring better performance and different topological designs, and the use of multiple filtering step is more suitable for SEMDOT than the single filtering step.
- The sensitivity analysis strategy adopted in SEMDOT is effective.

Table 8: Comparisons of topologies with different mesh sizes between SEMDOT and SEMDOT-S for L-bracket beam case

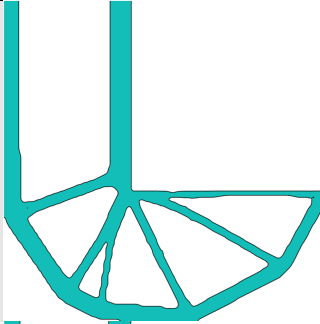
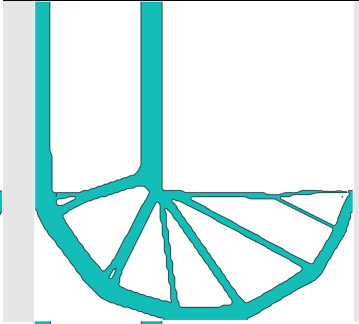
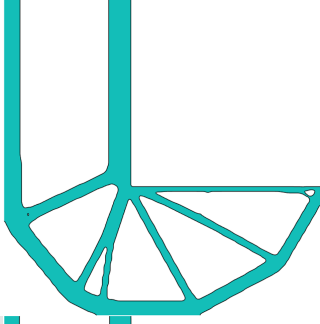

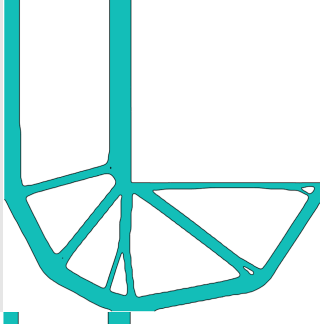
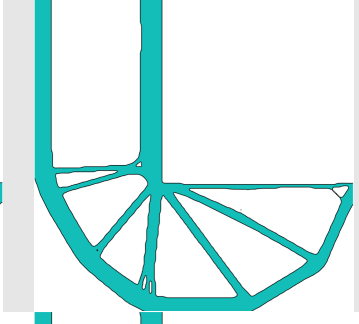
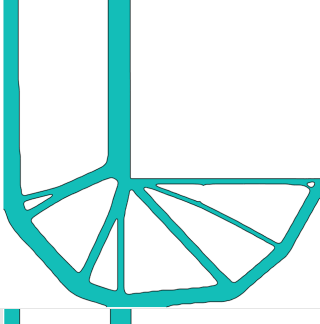
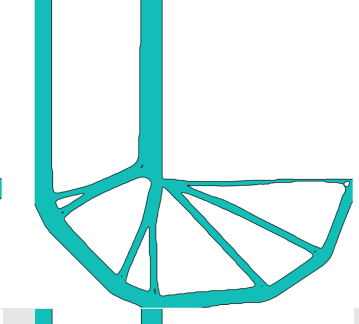
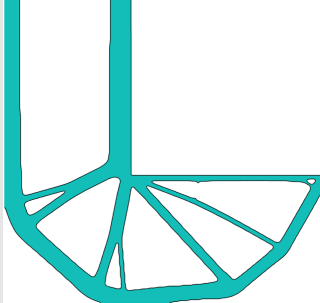
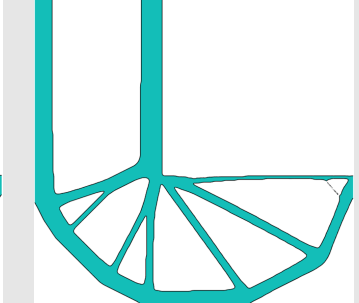
Mesh size	Algorithms	
	SEMDOT	SEMDOT-S
$L=150$		
$L=200$		
$L=250$		
$L=300$		
$L=350$		

Table 9: Effects of domain aspect ratio on compliance obtained by different algorithms solving L-bracket beam case

Algorithms	Domain aspect ratio					
	0.5:1	0.75:1	1.25:1	1.5:1	1.75:1	2:1
SEMDOT	254.4356	229.8695	245.7824	285.4968	314.0988	358.8990
SEMDOT-S	256.0683	232.1893	243.5014	285.5149	318.7357	360.8157
SIMP-D	297.6136	281.7546	317.8464	372.5226	449.1221	542.3667
SIMP-H	282.6777	322.5282	288.8244	355.5204	454.8071	498.2979
BESO	278.3044	253.3296	284.5204	335.2234	401.4278	490.0256
ETO	269.4174	244.8819	276.9958	321.1281	387.5802	476.9035

Table 10: Effects of domain aspect ratio on number of iterations obtained by different algorithms solving L-bracket beam case

Algorithms	Domain aspect ratio					
	0.5:1	0.75:1	1.25:1	1.5:1	1.75:1	2:1
SEMDOT	104	202	293	116	138	113
SEMDOT-S	128	300	192	148	130	122
SIMP-D	300	300	300	300	300	300
SIMP-H	181	234	213	201	214	230
BESO	71	68	78	77	78	68
ETO	97	90	218	89	98	90

- Even though SEMDOT is developed based on the SIMP framework, its convergency is stronger than standard SIMP because of its improved termination criteria.
- SEMDOT is capable of obtaining topological designs comparable or better than standard element-based algorithms such as SIMP and BESO or the newly developed ETO.

Even though this paper shows some benefits of SEMDOT, it should be acknowledged that when the same number of elements is used, the computational cost of SEMDOT would be higher than that of SIMP because of having to deal with extra grid points. It also should be acknowledged that SEMDOT is not a pioneering algorithm like SIMP, BESO, level-set method, MMC-based method, and using the floating projection. Instead, SEMDOT is an easy-to-use, flexible, and efficient optimization platform, which can be easily integrated with some existing approaches and solutions, particularly the ones developed for SIMP.

Funding

This research received no external funding.

Acknowledgements

The authors would like to thank Prof. Krister Svanberg for providing the MMA optimizer code. Mr. Yun-Fei Fu would like to thank Dr. Joe Alexandersen, University of Southern Denmark, for his suggestions on the mathematical statement of SEMDOT and Dr. Hongxin Wang, Hunan University, for his assistance on BESO test cases.

References

- [1] Z. H. Zuo, Y. M. Xie, A simple and compact Python code for complex 3D topology optimization, *Advances in Engineering Software* 85 (2015) 1–11.
- [2] L. N. S. Chiu, B. Rolfe, X. H. Wu, W. Y. Yan, Effect of stiffness anisotropy on topology optimisation of additively manufactured structures, *Engineering Structures* 171 (2018) 842–848.
- [3] N. Pollini, O. Sigmund, C. S. Andreasen, J. Alexandersen, A poor mans approach for high-resolution three-dimensional topology design for natural convection problems, *Advances in Engineering Software* 140 (2020) 102736.
- [4] M. P. Bendsøe, N. Kikuchi, Generating optimal topologies in structural design using a homogenization method, *Computer Methods in Applied Mechanics and Engineering* 71 (1988) 197–224.
- [5] M. P. Bendsøe, Optimal shape design as a material distribution problem, *Structural and Multidisciplinary Optimization* 1 (1989) 193–202.
- [6] Y. M. Xie, G. P. Steven, A simple evolutionary procedure for structural optimization, *Computers & Structures* 49 (1993) 885–896.
- [7] J. Sokolowski, A. Zochowski, On the topological derivative in shape optimization, *SIAM Journal on Control and Optimization* 37 (1999) 1251–1272.

- [8] G. Allaire, F. Jouve, A. M. Toader, A level-set method for shape optimization, *Comptes Rendus Mathematique* 334 (2002) 1125–1130.
- [9] M. Y. Wang, X. M. Wang, D. M. Guo, A level set method for structural topology optimization, *Computer Methods in Applied Mechanics and Engineering* 192 (2003) 227–246.
- [10] B. Bourdin, A. Chambolle, Design-dependent loads in topology optimization, *ESAIM: Control, Optimisation and Calculus of Variations* 9 (2003) 19–48.
- [11] X. Guo, W. S. Zhang, W. L. Zhong, Doing topology optimization explicitly and geometrically—A new moving morphable components based framework, *Journal of Applied Mechanics* 81 (2014) 081009.
- [12] W. S. Zhang, W. Y. Yang, J. H. Zhou, D. Li, X. Guo, Structural topology optimization through explicit boundary evolution, *Journal of Applied Mechanics* 84 (2017).
- [13] D. C. Da, L. Xia, G. Y. Li, X. D. Huang, Evolutionary topology optimization of continuum structures with smooth boundary representation, *Structural and Multidisciplinary Optimization* 57 (2018) 2143–2159.
- [14] X. D. Huang, Smooth topological design of structures using the floating projection, *Engineering Structures* 208 (2020) 110330.
- [15] X. D. Huang, On smooth or 0/1 designs of the fixed-mesh element-based topology optimization, *arXiv preprint arXiv:2006.04306* (2020).
- [16] Z. D. Ma, N. Kikuchi, I. Hagiwara, Structural topology and shape optimization for a frequency response problem, *Computational Mechanics* 13 (1993) 157–174.
- [17] Z. H. Zuo, Y. M. Xie, X. D. Huang, Evolutionary topology optimization of structures with multiple displacement and frequency constraints, *Advances in Structural Engineering* 15 (2012) 359–372.
- [18] C. Le, J. Norato, T. Bruns, C. Ha, D. Tortorelli, Stress-based topology optimization for continua, *Structural and Multidisciplinary Optimization* 41 (2010) 605–620.
- [19] D. M. De Leon, J. Alexandersen, J. S. Fonseca, O. Sigmund, Stress-constrained topology optimization for compliant mechanism design, *Structural and Multidisciplinary Optimization* 52 (2015) 929–943.
- [20] J. Alexandersen, N. Aage, C. S. Andreasen, O. Sigmund, Topology optimisation for natural convection problems, *International Journal for Numerical Methods in Fluids* 76 (2014) 699–721.
- [21] J. Alexandersen, O. Sigmund, N. Aage, Large scale three-dimensional topology optimisation of heat sinks cooled by natural convection, *International Journal of Heat and Mass Transfer* 100 (2016) 876–891.
- [22] J. Asmussen, J. Alexandersen, O. Sigmund, C. S. Andreasen, A poor mans approach to topology optimization of natural convection problems, *Structural and Multidisciplinary Optimization* 59 (2019) 1105–1124.
- [23] K. Nabaki, J. H. Shen, X. D. Huang, Evolutionary topology optimization of continuum structures considering fatigue failure, *Materials & Design* 166 (2019) 107586.
- [24] H. X. Wang, J. Liu, G. L. Wen, Y. M. Xie, The robust fail-safe topological designs based on the von Mises stress, *Finite Elements in Analysis and Design* 171 (2020) 103376.

- [25] N. Aage, E. Andreassen, B. S. Lazarov, Topology optimization using PETSc: An easy-to-use, fully parallel, open source topology optimization framework, *Structural and Multidisciplinary Optimization* 51 (2015) 565–572.
- [26] N. Aage, B. S. Lazarov, Parallel framework for topology optimization using the method of moving asymptotes, *Structural and Multidisciplinary Optimization* 47 (2013) 493–505.
- [27] H. X. Wang, J. Liu, G. L. Wen, An efficient evolutionary structural optimization method for multi-resolution designs, *Structural and Multidisciplinary Optimization* (2020) 1–17. doi:<https://doi.org/10.1007/s00158-020-02536-0>.
- [28] J. S. Jensen, O. Sigmund, Topology optimization for nano-photonics, *Laser & Photonics Reviews* 5 (2011) 308–321.
- [29] W. Chen, X. D. Huang, Topological design of 3D chiral metamaterials based on couple-stress homogenization, *Journal of the Mechanics and Physics of Solids* 131 (2019) 372–386.
- [30] J. K. Liu, Y. S. Ma, A survey of manufacturing oriented topology optimization methods, *Advances in Engineering Software* 100 (2016) 161–175.
- [31] S. L. Vatanabe, T. N. Lippi, C. R. de Lima, G. H. Paulino, E. C. Silva, Topology optimization with manufacturing constraints: A unified projection-based approach, *Advances in Engineering Software* 100 (2016) 97–112.
- [32] J. K. Liu, Piecewise length scale control for topology optimization with an irregular design domain, *Computer Methods in Applied Mechanics and Engineering* 351 (2019) 744–765.
- [33] M. Langelaar, Topology optimization for multi-axis machining, *Computer Methods in Applied Mechanics and Engineering* 351 (2019) 226–252.
- [34] H. C. Yu, J. Q. Huang, B. Zou, W. Shao, J. K. Liu, Stress-constrained shell-lattice infill structural optimisation for additive manufacturing, *Virtual and Physical Prototyping* 15 (2020) 35–48.
- [35] O. Sigmund, J. Petersson, Numerical instabilities in topology optimization: A survey on procedures dealing with checkerboards, mesh-dependencies and local minima, *Structural Optimization* 16 (1998) 68–75.
- [36] X. Y. Yang, Y. M. Xie, G. P. Steven, O. M. Querin, Bidirectional evolutionary method for stiffness optimization, *AIAA Journal* 37 (1999) 1483–1488.
- [37] K. Ghabraie, Y. M. Xie, X. D. Huang, G. Ren, Shape and reinforcement optimization of underground tunnels, *Journal of Computational Science and Technology* 4 (2010) 51–63.
- [38] K. Ghabraie, R. Chan, X. D. Huang, Y. M. Xie, Shape optimization of metallic yielding devices for passive mitigation of seismic energy, *Engineering Structures* 32 (2010) 2258–2267.
- [39] D. D. Liu, L. N. S. Chiu, C. Davies, W. Y. Yan, A post-processing method to remove stress singularity and minimize local stress concentration for topology optimized designs, *Advances in Engineering Software* 145 (2020) 102815.
- [40] Y. F. Chen, F. Meng, G. Y. Li, X. D. Huang, Topology optimization of photonic crystals with exotic properties resulting from dirac-like cones, *Acta Materialia* 164 (2019) 377–389.

- [41] B. S. Liu, D. Guo, C. Jiang, G. Y. Li, X. D. Huang, Stress optimization of smooth continuum structures based on the distortion strain energy density, *Computer Methods in Applied Mechanics and Engineering* 343 (2019) 276–296.
- [42] W. B. Li, F. Meng, Y. F. Li, X. D. Huang, Topological design of 3D phononic crystals for ultra-wide omnidirectional bandgaps, *Structural and Multidisciplinary Optimization* 60 (2019) 2405–2415.
- [43] Y. F. Fu, B. Rolfe, N. S. L. Chiu, Y. N. Wang, X. D. Huang, K. Ghabraie, Design and experimental validation of self-supporting topologies for additive manufacturing, *Virtual and Physical Prototyping* 14 (2019) 382–394.
- [44] Y. F. Fu, B. Rolfe, N. S. L. Chiu, Y. N. Wang, X. D. Huang, K. Ghabraie, Topology optimization of continuum structures using smooth boundary representation, in: *Proceedings of the 13th World Congress of Structural and Multidisciplinary Optimization Continued*, Beijing, China, 2019, pp. 448–454.
- [45] Y. F. Fu, B. Rolfe, N. S. L. Chiu, Y. N. Wang, X. D. Huang, K. Ghabraie, Parametric studies and manufacturability experiments on smooth self-supporting topologies, *Virtual and Physical Prototyping* 15 (2020) 22–34.
- [46] Y. F. Fu, B. Rolfe, N. S. L. Chiu, Y. N. Wang, X. D. Huang, K. Ghabraie, Smooth topological design of 3D continuum structures using elemental volume fractions, *Computers and Structures* 231 (2020) 106213.
- [47] T. H. Nguyen, G. H. Paulino, J. Song, C. H. Le, A computational paradigm for multiresolution topology optimization (MTOP), *Structural and Multidisciplinary Optimization* 41 (2010) 525–539.
- [48] J. Park, A. Sutradhar, A multi-resolution method for 3D multi-material topology optimization, *Computer Methods in Applied Mechanics and Engineering* 285 (2015) 571–586.
- [49] D. K. Gupta, M. Langelaar, F. van Keulen, QR-patterns: Artefacts in multiresolution topology optimization, *Structural and Multidisciplinary Optimization* 58 (2018) 1335–1350.
- [50] Z. Kang, Y. Q. Wang, Structural topology optimization based on non-local shepard interpolation of density field, *Computer Methods in Applied Mechanics and Engineering* 200 (2011) 3515–3525.
- [51] M. Langelaar, An additive manufacturing filter for topology optimization of print-ready designs, *Structural and Multidisciplinary Optimization* 55 (2017) 871–883.
- [52] Y. F. Fu, K. Ghabraie, B. Rolfe, Y. N. Wang, L. N. S. Chiu, X. D. Huang, Optimizing 3D Self-Supporting Topologies for Additive Manufacturing, in: *Proceedings of the 12th International Conference on Computer Modeling and Simulation*, 2020, pp. 220–223.
- [53] E. van de Ven, R. Maas, C. Ayas, M. Langelaar, F. van Keulen, Continuous front propagation-based overhang control for topology optimization with additive manufacturing, *Structural and Multidisciplinary Optimization* 57 (2018) 2075–2091.
- [54] K. Q. Zhang, G. D. Cheng, L. Xu, Topology optimization considering overhang constraint in additive manufacturing, *Computers & Structures* 212 (2019) 86–100.
- [55] X. Guo, J. H. Zhou, W. S. Zhang, Z. L. Du, C. Liu, Y. Liu, Self-supporting structure design in additive manufacturing through explicit topology optimization, *Computer Methods in Applied Mechanics and Engineering* 323 (2017) 27–63.

- [56] K. Ghabraie, An improved soft-kill BESO algorithm for optimal distribution of single or multiple material phases, *Structural and Multidisciplinary Optimization* 52 (2015) 773–790.
- [57] K. Ghabraie, The ESO method revisited, *Structural and Multidisciplinary Optimization* 51 (2015) 1211–1222.
- [58] M. P. Bendsøe, O. Sigmund, *Topology Optimization Theory, Method and Applications*, 2nd ed., Springer-Verlag, Berlin Heidelberg, 2004.
- [59] X. D. Huang, Y. Li, S. W. Zhou, Y. M. Xie, Topology optimization of compliant mechanisms with desired structural stiffness, *Engineering Structures* 79 (2014) 13–21.
- [60] B. L. Zhu, X. M. Zhang, H. C. Zhang, J. W. Liang, H. Y. Zang, H. Li, R. X. Wang, Design of compliant mechanisms using continuum topology optimization: A review, *Mechanism and Machine Theory* 143 (2020) 103622.
- [61] B. S. Lazarov, O. Sigmund, Filters in topology optimization based on Helmholtz-type differential equations, *International Journal for Numerical Methods in Engineering* 86 (2011) 765–781.
- [62] O. Sigmund, Morphology-based black and white filters for topology optimization, *Structural and Multidisciplinary Optimization* 33 (2007) 401–424.
- [63] O. Sigmund, On the design of compliant mechanisms using topology optimization, *Journal of Structural Mechanics* 25 (1997) 493–524.
- [64] J. K. Guest, J. H. Prévost, T. Belytschko, Achieving minimum length scale in topology optimization using nodal design variables and projection functions, *International Journal for Numerical Methods in Engineering* 61 (2004) 238–254.
- [65] S. L. Xu, Y. W. Cai, G. D. Cheng, Volume preserving nonlinear density filter based on heaviside functions, *Structural and Multidisciplinary Optimization* 41 (2010) 495–505.
- [66] X. D. Huang, Y. M. Xie, Convergent and mesh-independent solutions for the bi-directional evolutionary structural optimization method, *Finite Elements in Analysis and Design* 43 (2007) 1039–1049.
- [67] F. W. Wang, B. S. Lazarov, O. Sigmund, On projection methods, convergence and robust formulations in topology optimization, *Structural and Multidisciplinary Optimization* 43 (2011) 767–784.
- [68] L. Xia, Q. Xia, X. D. Huang, Y. M. Xie, Bi-directional evolutionary structural optimization on advanced structures and materials: A comprehensive review, *Archives of Computational Methods in Engineering* 25 (2018) 437–478.
- [69] O. Sigmund, K. Maute, Topology optimization approaches: A comparative review, *Structural and Multidisciplinary Optimization* 48 (2013) 1031–1055.
- [70] O. Sigmund, A 99 line topology optimization code written in Matlab, *Structural and Multidisciplinary Optimization* 21 (2001) 120–127.
- [71] K. Svanberg, The method of moving asymptotes (MMA) with some extensions, in: G. I. N. Rozvany (Ed.), *Optimization of Large Structural Systems*, Springer, Dordrecht: Kluwer, 1993, pp. 555–566.
- [72] E. Andreassen, A. Clausen, M. Schevenels, B. S. Lazarov, O. Sigmund, Efficient topology optimization in MATLAB using 88 lines of code, *Structural and Multidisciplinary Optimization* 43 (2011) 1–16.

- [73] X. D. Huang, Y. M. Xie, A further review of ESO type methods for topology optimization, *Structural and Multidisciplinary Optimization* 41 (2010) 671–683.
- [74] B. Bourdin, Filters in topology optimization, *International Journal for Numerical Methods in Engineering* 50 (2001) 2143–2158.
- [75] T. E. Bruns, D. A. Tortorelli, Topology optimization of non-linear elastic structures and compliant mechanisms, *Computer Methods in Applied Mechanics and Engineering* 190 (2001) 3443–3459.
- [76] K. Liu, A. Tovar, An efficient 3D topology optimization code written in Matlab, *Structural and Multidisciplinary Optimization* 50 (2014) 1175–1196.

Appendix: Matlab Code of SEMDOT

The 2D code of SEMDOT was written based on the Matlab codes presented by Andreassen et al. [72] and Huang and Xie [73]. To use the MMA optimizer, two additional files: `mmasub.m` and `subsolv.m`, which can be obtained by contacting Prof. Krister Svanberg from KTH in Stockholm Sweden, are needed. The implementation of SEMDOT is not limited to the code provided here. The code should be regarded as a reference, and therefore the readers are encouraged to improve the code based on the idea of SEMDOT. In addition, the 2D Matlab code of SEMDOT can be easily extended to a 3D version based on the 169 line code presented by Liu and Tovar [76].

```

1  %%%% A Matlab Code for SEMDOT Algorithm %%%%
2  function SEMDOT(nelx , nely , vol , rmin , nG)
3  % Author One: Yun-Fei Fu <fuyunf@deakin.edu.au>
4  % Topology Optimization Group
5  % School of Engineering , Deakin University
6  % Author Two: Prof. Xiaodong Huang <xhuang@swin.edu.au>
7  % School of Engineering , Swinburne University of Technology
8  % Advisors: Dr. Kazem Ghabraie; Prof. Bernard Rolfe; Dr. Yanan Wang;
9  % Dr. Louis N.S. Chiu
10 % Date Created: 12/08/18
11 % Date last modified: 03/01/20
12 % Description:
13 % This function SEMDOT implements Smooth-Edged Material Distribution for
14 % Optimizing Topology (SEMDOT) algorithm
15
16 %%% Disclaimer:
17 %%% This code is provided for educational or academic purposes and is not
18 %%% guaranteed to be free of errors. The authors are not liable for any
19 %%% problems caused by the use of this code.
20
21 % INPUT:
22 % nelx: The number of elements in the horizontal direction.
23 % nely: The number of elements in the vertical direction.
24 % vol: The prescribed value of the allowable volume.
25 % rmin: The predefined filter radius.

```

```

26 % nG: The number of grid points assigned to each element.
27
28 % OUTPUT:
29 % It.: The iteration number.
30 % Obj.: The value of compliance.
31 % Vol.: The volume fraction.
32 % ch.: The computational error.
33 % Topo.: The topological error.
34 % contourf(fnx, flipud(fny), xg-ls, [0 0]) shows optimized topologies.
35
36 %% INITIALIZATION
37 vx = repmat(vol,nely,nelx); vxPhys = vx; change = 1; loop = 0;
38 Emin = 0.001; maxloop = 1000; ngrid = nG-1; tolx = 0.001;
39 E0 = 1; nu = 0.3; penal = 1.5; rnmin = 1;
40 %% INITIALIZE MMA OPTIMIZER
41 nele = nely*nelx; m = 1; n = nely*nelx; nelm = nely*nelx;
42 vxmin = 1e-3*ones(nelm,1); vxmax = ones(nelm,1);
43 vxold1 = reshape(vx,nelm,1); vxold2 = vxold1;
44 a0 = 1; ai = 0; ci = 1000; di = 0; low = ones(nelm,1); upp = 1;
45 %% INITIALIZE HEAVISIDE SMOOTH FUNCTION
46 beta = 0.5; ER = 0.5;
47 %% PREPARE FINITE ELEMENT ANALYSIS
48 A11 = [12 3 -6 -3; 3 12 3 0; -6 3 12 -3; -3 0 -3 12];
49 A12 = [-6 -3 0 3; -3 -6 -3 -6; 0 -3 -6 3; 3 -6 3 -6];
50 B11 = [-4 3 -2 9; 3 -4 -9 4; -2 -9 -4 -3; 9 4 -3 -4];
51 B12 = [ 2 -3 4 -9; -3 2 9 -2; 4 9 2 3; -9 -2 3 2];
52 KE = 1/(1-nu^2)/24*([A11 A12;A12' A11]+nu*[B11 B12;B12' B11]);
53 nodenrs = reshape(1:(1+nelx)*(1+nely),1+nely,1+nelx);
54 edofVec = reshape(2*nodenrs(1:end-1,1:end-1)+1,nelx*nely,1);
55 edofMat = repmat(edofVec,1,8)+repmat([0 1 2*nely+[2 3 0 1] -2 -1],nelx*nely,1);
56 iK = reshape(kron(edofMat,ones(8,1))',64*nelx*nely,1);
57 jK = reshape(kron(edofMat,ones(1,8))',64*nelx*nely,1);
58 %% ELEMENTAL NODES AND COORDINATES
59 [nodex,nodey] = meshgrid(0:nelx,0:nely);
60 [fnx,fny] = meshgrid(0:1/ngrid:nelx,0:1/ngrid:nely);
61 %% DEFINE LOADS AND SUPPORTS (CANTILEVER BEAM)
62 F = sparse(2*(nely+1)*(nelx+1)-nely,1,-1,2*(nely+1)*(nelx+1),1);
63 fixeddofs = (1:2*(nely+1));
64 U = zeros(2*(nely+1)*(nelx+1),1);
65 alldofs = [1:2*(nely+1)*(nelx+1)];
66 freedofs = setdiff(alldofs,fixeddofs);
67 %% PREPARE FILTER FOR ELEMENT
68 iH = ones(nelx*nely*(2*(ceil(rnmin)-1)+1)^2,1);

```

```

69 jH = ones(size(iH));
70 sH = zeros(size(iH));
71 k = 0;
72 for i1 = 1:nex
73     for j1 = 1:nely
74         e1 = (i1-1)*nely+j1;
75         for i2 = max(i1-(ceil(rmin)-1),1):min(i1+(ceil(rmin)-1),nex)
76             for j2 = max(j1-(ceil(rmin)-1),1):min(j1+(ceil(rmin)-1),nely)
77                 e2 = (i2-1)*nely+j2;
78                 k = k+1;
79                 iH(k) = e1;
80                 jH(k) = e2;
81                 sH(k) = max(0,rmin-sqrt((i1-i2)^2+(j1-j2)^2));
82             end
83         end
84     end
85 end
86 H = sparse(iH,jH,sH); Hs = sum(H,2);
87 %% PREPARE FILTER FOR NODALS
88 inH = ones((nex+1)*(nely+1)*(2*(ceil(rnmin)+1))^2,1);
89 jnH = ones(size(inH)); snH = zeros(size(inH)); k = 0;
90 [elex,eley] = meshgrid(1.5:nex+0.5,1.5:nely+0.5);
91 for in1 = 1:nex+1
92     for jn1 = 1:nely+1
93         en1 = (in1-1)*(nely+1)+jn1;
94         for in2 = max(in1-ceil(rnmin),1):min(in1+ceil(rnmin)-1,nex)
95             for jn2 = max(jn1-ceil(rnmin),1):min(jn1+ceil(rnmin)-1,nely)
96                 en2 = (in2-1)*nely+jn2; k = k+1; inH(k) = en1;
97                 jnH(k) = en2;
98                 snH(k) = max(0,rnmin-sqrt((in1-elex(jn2,in2))^2+(jn1-eley(jn2,in2))^2));
99             end
100         end
101     end
102 end
103 Hn = sparse(inH,jnH,snH); Hns = sum(Hn,2);
104 %% START ITERATION
105 while (change > tolx || tol > 0.001) && loop < maxloop
106     loop = loop+1;
107     %% FE-ANALYSIS
108     sK = reshape(KE(:)*(vxPhys(:)'*E0+(1-vxPhys(:))'*(Emin^penal*E0)),64*nex*nely,1);
109     K = sparse(iK,jK,sK); K = (K+K')/2;

```

```

110 U(freedofs) = K(freedofs, freedofs)\F(freedofs);
111 %% OBJECTIVE FUNCTION AND SENSITIVITY ANALYSIS
112 ce = reshape(sum((U(edofMat)*KE).*U(edofMat)), 2, nely, nelx);
113 c(loop) = sum(sum((vxPhys.*E0+(1-vxPhys).*(Emin^penal*E0)).*ce));
114 dc = -penal*((1-vxPhys)*Emin.^(penal-1)+vxPhys).*E0.*ce;
115 dv = ones(nely, nelx);
116 %% FILTERING/MODIFICATION OF SENSITIVITIES
117 dc(:) = H*(dc(:)./Hs);
118 dv(:) = H*(dv(:)./Hs);
119 %% UPDATE DESIGN VARIABLES AND FILTERED ELEMENTAL VOLUME FRACTIONS
120 vxval = reshape(vx, nelm, 1);
121 fval = sum(vxPhys(:))/(vol*nely*nelx)-1;
122 dfdx = dv(:)'/ (vol*nely*nelx);
123 f0val = c;
124 df0dx = dc(:);
125 [vxmma,~,~,~,~,~,~,~,~,low,upp] = ...
126     mmasub(m,n,loop,vxval,vxmin,vxmax,vxold1,vxold2,f0val,df0dx,fval,dfdx,low,
127         upp,a0,ai,ci,di);
128 vxnew = reshape(vxmma,nely,nelx);
129 vxPhys(:) = (H*vxnew(:))./Hs;
130 vxold2 = vxold1(:);
131 vxold1 = vx(:);
132 %% ASSIGN FILTERED ELEMENTAL VOLUME FRACTIONS TO NODAL DENSITIES
133 xn = reshape((Hn*vxPhys(:)./Hns), nely+1, nelx+1);
134 %% UPDATE POINT DESNGY BY A HEAVISIDE SMOOTH/STEP FUNCTION
135 xg = interp2(nodex, nodey, xn, fnx, fny, 'linear');
136 l1 = 0; l2 = 1;
137 while (l2-l1) > 1.0e-5
138     ls = (l1+l2)/2.0;
139     xgnew = max(0.001, (tanh(beta*ls)+tanh(beta*(xg-ls)))/(tanh(beta*ls)+tanh(
140         beta*(1-ls))));
141     if sum(sum(xgnew))/((ngrid*nelx+1)*(ngrid*nely+1)) - sum(vxPhys(:))/(nelx*
142         nely) > 0
143         l1 = ls;
144     else
145         l2 = ls;
146     end
147 end
148 %% ASSEMBLE GRID POINTS TO ELEMENTS
149 vxPhys(:) = 0;
150 Terr = 0;
151 Tm = [];
152 for i = 1:nelx

```

```

150     for j = 1:nely
151         e = (i-1)*nely + j;
152         for i1 = ngrid*(i-1)+1:ngrid*i+1
153             for j1 = ngrid*(j-1)+1:ngrid*j+1
154                 Tm = [Tm; xgnew(j1, i1)];
155                 vxPhys(e) = vxPhys(e)+xgnew(j1, i1);
156             end
157         end
158         if min(Tm) > 0.001 && max(Tm) < 1
159             Terr = Terr+1;
160         end
161         Tm = [];
162     end
163 end
164 vxPhys = vxPhys/(ngrid+1)^2;
165 %% CHECK CONVERGENCE
166 change = sum(abs(vxnew(:)-vx(:)))/(vol*nely*nex);
167 tol = Terr/nele;
168 vx = vxnew;
169 %% PLOT RESULTS
170 fprintf('It.:%3i Obj.:%8.4f Vol.:%4.3f ch.:%4.5f Topo.:%7.5f\n\n', loop, c(loop),
        mean(vxPhys(:)), change, tol);
171 contourf(fnx, flipud(fny), xg-1s, [0 0]);
172 axis equal; axis tight; axis off; pause(1e-6);
173 %% UPDATE HEAVISIDE SMOOTH FUNCTION
174 beta = beta+ER; fprintf('Parameter beta increased to %g.\n', beta);
175 end

```